Geophys. J. Int. (2006) **165,** 744–762 doi: 10.1111/j.1365-246X.2005.02816.x

An integral equation approach for 2.5-dimensional forward and inverse electromagnetic scattering

Aria Abubakar, Peter M van den Berg* and Tarek M Habashy

Schlumberger-Doll Research, 36 *Old Quarry Road, Ridgefield,* CT-06877*, USA. E-mail: AAbubakar@slb.com*

Accepted 2005 September 21. Received 2005 July 3; in original form 2005 March 11

SUMMARY

We present 2.5-D forward and inverse algorithms for modelling low-frequency electromagnetic scattering problems. These algorithms are intended to be used for interpretation of large-scale electromagnetic geophysical data. The algorithms are based on an integral equation approach. To solve the forward problem, a standard conjugate gradient normal residual method is employed, while the inverse problem is solved with the so-called multiplicative regularized contrast source inversion method. Inversion results with low-frequency electromagnetic data for single- and cross-well configurations are presented. Furthermore the advantages of combining the long-offset single-well and cross-well data are discussed.

Key words: electromagnetic induction, inverse problem, perturbation method, numerical techniques.

1 INTRODUCTION

To extend the sensitivity of this electromagnetic technology, in the last decade, alternative technologies such as the low-frequency electromagnetic cross-well logging Wilt *et al.* (1995); Alumbaugh & Newman (1997); Abubakar & van den Berg (2000); Zhdanov & Yoshioka (2003) and the long-offset single-well logging (Alumbaugh & Wilt 2001) have been developed. By using these technologies the conductivity map for the region beyond a couple of metres from the wells can be obtained. In the cross-well logging, when the measurements are collected using only two adjacent wells the use of full 3-D inversion approach is not recommended, since only the conductivity distribution on the cross-section between the two wells can be determined reliably (Spies & Habashy 1995). We, therefore, have to reduce the number of unknown conductivity parameters to meet the limited amount of available measurement data. One obvious possibility is to assume that the configuration is invariant in the direction orthogonal to the plane of observation. However, since we are working in the low-frequency regime (diffusive), the 2-D approximation of the electromagnetic scattering problem at hand will lead to incorrect results, because the electromagnetic field of magnetic dipole sources will maintain its 3-D character. Especially in the near field region, which is always the case in our applications, the electromagnetic fields behaviour in 3-D and in 2-D are completely different, see Allers *et al.* (1994); Druskin & Knizhnerman (1994); Torres-Verdin & Habashy (1994).

We, therefore, consider the so-called 2.5-D problem, where the configuration is 2-D, but the electromagnetic field is treated in a full vector 3-D fashion. Unlike other 2.5-D algorithms Allers *et al.* (1994); Druskin & Knizhnerman (1994); Torres-Verdin & Habashy (1994), in this paper we use a full integral equation (IE) approach to solve the 2.5-D forward and inverse scattering problems. Using a spatial Fourier transformation with respect to the coordinate in the invariant direction, the 3-D electromagnetic field problem is reduced to a number of 2-D problems. Since we are only interested in the field in the cross-section of the plane of observation, it is anticipated that the 2-D forward problem and 2-D inverse problems have to be solved only for a few Fourier spectral parameters.

We first discuss the solution of the 2.5-D forward problem. We assume that the conductivity in a bounded domain differs from the constant conductivity of the background medium. This is mathematically expressed by stating that the conductivity in a bounded domain exhibits a conductivity contrast with respect to the one of the background medium. After Fourier transformation in the invariant direction, for each Fourier parameter, the problem is reduced to the problem of solving a 2-D IE over the domain of the contrasting conductivity. In view of the later work for the inverse scattering problem, we solve this 2.5-D IE by a conjugate gradient for normal residual (CGNR) method (van den Berg 1984). In fact all the 2-D problems of each Fourier parameter are solved simultaneously. After that the inverse Fourier transformation

*On temporary leave from the Faculty of Applied Sciences, Delft University of Technology, 2628 CJ Delft, the Netherlands.

is carried out to obtain the electromagnetic fields at the points of observation. Some numerical experiments are carried out to investigate the influence of the discretization in the Fourier domain on the forward modelling results.

Second, we formulate the 2.5-D inverse scattering problem in terms of the contrast source IEs (Habashy *et al.* 1990, 1994). The inversion method used in this paper is known as the contrast source inversion (CSI) method (van den Berg & Kleinman 1997). In this CSI method, the unknown contrast sources (the internal fields multiplied by the contrasts) and the unknown contrasts are reconstructed by minimization of a cost functional. This cost functional is the weighted sum of the error norm in matching the model to the data and the error norm in satisfying of the IE inside the domain of interest. Earlier, Zhdanov & Chernyak (1987) have proposed an inversion scheme based on an unweighted sum of these error norms, but ample experience has shown that the proper weighting is essential to the success of the CSI method and its application to present problem. The minimization procedure is carried in two alternate steps:

(a) the contrast sources are updated via a CG direction of the cost functional and
(b) the contrasts are found by direct minimization of the appropriate terms in the cost functional, which is equivalent to find the least-square fit of the constitutive relations between the contrast sources and the internal fields. In this way the total complexity of each iteration in the CSI method is approximately equal to the complexity of two iterations of the CG of the equivalent forward problems.

When the number of data is very limited and a significant noise level is present in the data, which is always the case in our applications, the CSI method will not provide one with a reasonable resolution of the reconstruction results. Hence, in the work reported in this paper we will employ the weighted L^2-norm regularizer as a multiplicative constraint in our CSI method (Abubakar *et al.* 2003). This regularization factor has all the advantages of the total variation regularization term (Vogel 2002), however, this factor is a L^2-norm (quadratic functional). The main advantage of using this multiplicative constraint is that the weighting parameter of the regularization factor used in the inversion algorithm is determined automatically by the optimization process. This significantly increases the robustness of the inversion method. This method is denoted as the multiplicative regularized CSI method (MR-CSI).

As numerical examples we present inversion from the cross-well and the long-offset single-well measurement system. In the cross-well inversion the advantage of using the source–receiver reciprocity will be demonstrated. Further some advantages of using joint inversion of cross-well and single-well data either sequentially or simultaneously will also be discussed.

2 THE SCATTERING PROBLEM

We consider an IE formulation of the electromagnetic problem. We assume that a non-magnetic scatterer with support $D^{\rm sct}$ is located in a homogeneous background medium with permeability μ_0 and electrical conductivity σ_0. We define an object domain D such that $D^{\rm sct} \in D$. A Cartesian coordinate system is centred in D with a position vector denoted by $\boldsymbol{x} = (x_1, x_2, x_3)$. The problem is invariant along the x_2-direction. We, therefore, introduce the transverse position vector $\boldsymbol{x}_T = (x_1, x_3)$. The scattering problem is formulated in the frequency domain with a time factor $\exp(-\mathrm{i}\omega t)$, where ω is the angular frequency and t is the time. We assume that the frequency is sufficiently low to neglect the displacement current. Consequently, the wavenumber of the background medium is given by $k_0 = (\mathrm{i}\omega\mu_0\sigma_0)^{\frac{1}{2}}$, where $\mathrm{Re}(k_0) > 0$. The object domain D is characterized by a contrast function defined as follows:

$$\chi(\boldsymbol{x}_T) = \frac{\sigma(\boldsymbol{x}_T)}{\sigma_0} - 1\,, \tag{1}$$

where $\sigma(\boldsymbol{x}_T)$ is the spatially dependent electrical conductivity (S/m).

In order to take advantage of the 2-D structure of the configuration, we introduce the 1-D spatial Fourier transform and its inverse with respect to the x_2-coordinate as follows:

$$\tilde{u} = \mathcal{F}\{u\} = \int_{x_2=-\infty}^{\infty} \exp(\mathrm{i}k_2 x_2) u(\boldsymbol{x}_T, x_2)\, dx_2\,, \tag{2}$$

$$u = \mathcal{F}^{-1}\{\tilde{u}\} = \frac{1}{2\pi}\int_{k_2=-\infty}^{\infty} \exp(-\mathrm{i}k_2 x_2) \tilde{u}(\boldsymbol{x}_T, k_2)\, dk_2\,. \tag{3}$$

It is well known that the scattered electric field $\boldsymbol{E}^{\rm sct} = \boldsymbol{E}^{\rm sct}(\boldsymbol{x}_T, x_2)$ and the scattered magnetic field $\boldsymbol{H}^{\rm sct} = \boldsymbol{H}^{\rm sct}(\boldsymbol{x}_T, x_2)$ are given by de Hoop (1995):

$$\boldsymbol{E}^{\rm sct}(\boldsymbol{x}_T, x_2) = \left(k_0^2 + \boldsymbol{\nabla}\boldsymbol{\nabla}\cdot\right) \boldsymbol{A}(\boldsymbol{x}_T, x_2)\,, \tag{4}$$

$$\boldsymbol{H}^{\rm sct}(\boldsymbol{x}_T, x_2) = \sigma_0 \boldsymbol{\nabla} \times \boldsymbol{A}(\boldsymbol{x}_T, x_2)\,, \tag{5}$$

where the symbol $\boldsymbol{\nabla} = (\partial_1, \partial_2, \partial_3)$ denotes spatial differentiation with respect to the position vector $\boldsymbol{x}$. The normalized vector potential $\boldsymbol{A}$ is given by

$$\boldsymbol{A}(\boldsymbol{x}_T, x_2) = \int_{\boldsymbol{x}'_T \in D}^{\mathrm{dA}} \int_{x'_2=-\infty}^{\infty} dx'_2 G(\boldsymbol{x}_T - \boldsymbol{x}'_T, x_2 - x'_2)\chi(\boldsymbol{x}'_T)\boldsymbol{E}(\boldsymbol{x}'_T, x'_2), \tag{6}$$

where $\boldsymbol{E}(\boldsymbol{x}_T, x_2)$ denotes the total electric field and G denotes the Green function of the homogeneous background, where

$$G(\boldsymbol{x}_T, x_2) = \frac{\exp\left(\mathrm{i}k_0\sqrt{|\boldsymbol{x}_T|^2 + x_2^2}\right)}{4\pi\sqrt{|\boldsymbol{x}_T|^2 + x_2^2}} = \frac{1}{(2\pi)^3}\int_{\boldsymbol{k}\in\mathbb{R}^3} \frac{\exp(-\mathrm{i}\boldsymbol{k}\cdot\boldsymbol{x})}{\boldsymbol{k}\cdot\boldsymbol{k} - k_0^2}\, dV_k, \tag{7}$$

in which $\boldsymbol{k} = (k_1, k_2, k_3)$ is the 3-D Fourier transform parameter. In view of the fact that the contrast function χ is invariant in the x_2-direction, we transform eqs (4) and (5) to the 1-D spatial Fourier domain,

$$\tilde{\boldsymbol{E}}^{\mathrm{sct}}(\boldsymbol{x}_T, k_2) = \left(k_0^2 + \tilde{\boldsymbol{\nabla}}\tilde{\boldsymbol{\nabla}}\cdot\right)\tilde{\boldsymbol{A}}(\boldsymbol{x}_T, k_2), \tag{8}$$

$$\tilde{\boldsymbol{H}}^{\mathrm{sct}}(\boldsymbol{x}_T, k_2) = \sigma_0\tilde{\boldsymbol{\nabla}}\times\tilde{\boldsymbol{A}}(\boldsymbol{x}_T, k_2), \tag{9}$$

where $\tilde{\boldsymbol{\nabla}} = (\partial_1, -\mathrm{i}k_2, \partial_3)$. The transformed normalized vector potential is obtained as

$$\tilde{\boldsymbol{A}}(\boldsymbol{x}_T, k_2) = \int_{\boldsymbol{x}'_T\in D} \tilde{G}(\boldsymbol{x}_T - \boldsymbol{x}'_T, k_2)\chi(\boldsymbol{x}'_T)\tilde{\boldsymbol{E}}(\boldsymbol{x}'_T, k_2)\, dA, \tag{10}$$

where

$$\tilde{G}(\boldsymbol{x}_T, k_2) = \int_{x_2=-\infty}^{\infty} \exp(\mathrm{i}k_2 x_2) G(\boldsymbol{x}_T, x_2)\, dx_2. \tag{11}$$

Using eq. (7) in eq. (11) we obtain

$$\begin{aligned}\tilde{G}(\boldsymbol{x}_T, k_2) &= \frac{1}{(2\pi)^2}\int_{\boldsymbol{k}_T\in\mathbb{R}^2} \frac{\exp(-\mathrm{i}\boldsymbol{k}_T\cdot\boldsymbol{x}_T)}{\boldsymbol{k}_T\cdot\boldsymbol{k}_T - \left(k_0^2 - k_2^2\right)}\, dA_k \\ &= \frac{\mathrm{i}}{4}H_0^{(1)}\left[\gamma_0(k_2)\,|\boldsymbol{x}_T|\right],\end{aligned} \tag{12}$$

where $\gamma_0(k_2) = (k_0^2 - k_2^2)^{1/2}$ and $\boldsymbol{k}_T = (k_1, k_3)$. Before discussing the IE we first describe the incident field, which is the electromagnetic field from a magnetic dipole in a homogeneous background medium.

3 INCIDENT FIELD GENERATED BY A MAGNETIC DIPOLE SOURCE

The electromagnetic field from a magnetic dipole with magnetic moment, $\boldsymbol{M}$, located at $\{x_1^S, x_3^S, 0\}$ in the homogeneous background medium is obtained as follows:

$$\boldsymbol{E}^{\mathrm{inc}}(\boldsymbol{x}_T, x_2) = -\boldsymbol{\nabla}G\left(\boldsymbol{x}_T - \boldsymbol{x}_T^S, x_2\right)\times\boldsymbol{M}, \tag{13}$$

$$\boldsymbol{H}^{\mathrm{inc}}(\boldsymbol{x}_T, x_2) = -\frac{1}{\mathrm{i}\omega\mu_0}\left(k_0^2 + \boldsymbol{\nabla}\boldsymbol{\nabla}\cdot\right)G\left(\boldsymbol{x}_T - \boldsymbol{x}_T^S, x_2\right)\boldsymbol{M}. \tag{14}$$

For the IEs discussed in the next section, we need the Fourier transform of the incident electric field inside the object domain ($\boldsymbol{x}\in D$), which directly follows from eq. (13). The Fourier transform of this field is obtained as

$$\tilde{\boldsymbol{E}}^{\mathrm{inc}}(\boldsymbol{x}_T, k_2) = -\tilde{\boldsymbol{\nabla}}\tilde{G}\left(\boldsymbol{x}_T - \boldsymbol{x}_T^S, k_2\right)\times\boldsymbol{M}. \tag{15}$$

For different orientations of a magnetic dipole with unit magnetic moment, the incident electric field components in the 1-D spatial Fourier domain are given by

$$\begin{cases}\tilde{E}_1^{\mathrm{inc}}(\boldsymbol{x}_T, k_2) = 0, \\ \tilde{E}_2^{\mathrm{inc}}(\boldsymbol{x}_T, k_2) = -\partial_3\tilde{G}\left(\boldsymbol{x}_T - \boldsymbol{x}_T^S, k_2\right), \quad \boldsymbol{M} = \{1, 0, 0\}, \\ \tilde{E}_3^{\mathrm{inc}}(\boldsymbol{x}_T, k_2) = -\mathrm{i}k_2\tilde{G}\left(\boldsymbol{x}_T - \boldsymbol{x}_T^S, k_2\right),\end{cases}$$

$$\begin{cases}\tilde{E}_1^{\mathrm{inc}}(\boldsymbol{x}_T, k_2) = \partial_3\tilde{G}\left(\boldsymbol{x}_T - \boldsymbol{x}_T^S, k_2\right), \\ \tilde{E}_2^{\mathrm{inc}}(\boldsymbol{x}_T, k_2) = 0, \qquad\qquad \boldsymbol{M} = \{0, 1, 0\}, \\ \tilde{E}_3^{\mathrm{inc}}(\boldsymbol{x}_T, k_2) = -\partial_1\tilde{G}\left(\boldsymbol{x}_T - \boldsymbol{x}_T^S, k_2\right),\end{cases}$$

$$\begin{cases}\tilde{E}_1^{\mathrm{inc}}(\boldsymbol{x}_T, k_2) = \mathrm{i}k_2\tilde{G}\left(\boldsymbol{x}_T - \boldsymbol{x}_T^S, k_2\right), \\ \tilde{E}_2^{\mathrm{inc}}(\boldsymbol{x}_T, k_2) = \partial_1\tilde{G}\left(\boldsymbol{x}_T - \boldsymbol{x}_T^S, k_2\right), \qquad \boldsymbol{M} = \{0, 0, 1\}, \\ \tilde{E}_3^{\mathrm{inc}}(\boldsymbol{x}_T, k_2) = 0,\end{cases} \tag{16}$$

where

$$\partial_1\tilde{G}\left(\boldsymbol{x}_T - \boldsymbol{x}_T^S, k_2\right) = -\frac{\left(x_1 - x_1^S\right)}{\left|\boldsymbol{x}_T - \boldsymbol{x}_T^S\right|}\,\gamma_0\frac{\mathrm{i}}{4}H_1^{(1)}\left[\gamma_0(k_2)\left|\boldsymbol{x}_T - \boldsymbol{x}_T^S\right|\right], \tag{17}$$

$$\partial_3\tilde{G}\left(\boldsymbol{x}_T - \boldsymbol{x}_T^S, k_2\right) = -\frac{\left(x_3 - x_3^S\right)}{\left|\boldsymbol{x}_T - \boldsymbol{x}_T^S\right|}\,\gamma_0\frac{\mathrm{i}}{4}H_1^{(1)}\left[\gamma_0(k_2)\left|\boldsymbol{x}_T - \boldsymbol{x}_T^S\right|\right]. \tag{18}$$

In the final step of solving the forward problem we have to transform the computed magnetic field components in the k_2-domain back to the spatial domain. Since we only have to know the total electric field $\{\tilde{E}_1, \tilde{E}_2, \tilde{E}_3\}$ in the spatial domain occupied by the scatterer, there is no need to know the electric field distribution very precisely in the whole space. Hence, it is sufficient that we have a good approximation for the electric field in the cross-section of the configuration where the electromagnetic sources are active. Therefore, we search for a very limited set of k_2-values such that in the inverse Fourier transform, for $x_2 = 0$, the infinite integral in the inverse Fourier transformation can be approximated by the finite summation

$$\boldsymbol{E}^{\text{inc}}(\boldsymbol{x}_T, 0) \approx \sum_{k_2} \beta(k_2) \tilde{\boldsymbol{E}}^{\text{inc}}(\boldsymbol{x}_T, k_2)\,. \tag{19}$$

For an uniform grid, $\beta(k_2) = \Delta k_2/2\pi$, where Δk_2 denotes the grid size in the Fourier domain. Examining the functional behaviour of $\tilde{\boldsymbol{E}}^{\text{inc}}(\boldsymbol{x}_T, k_2)$ as a function of k_2 we note that the largest values occur at $k_2 = \text{Re}(k_0)$. Hence, one of the grid nodes in the Fourier domain should coincide with the wavenumber value of $\text{Re}(k_0)$.

4 FORWARD SCATTERING PROBLEM

From eqs (8)–(10) we note that the scattered electric and magnetic fields are determined from the total electric field inside the object domain D. By assigning the observation point $\boldsymbol{x}_T$ to be inside the object domain D and by using the superposition principle,

$$\tilde{\boldsymbol{E}}^{\text{inc}}(\boldsymbol{x}_T, k_2) = \tilde{\boldsymbol{E}}(\boldsymbol{x}_T, k_2) - \tilde{\boldsymbol{E}}^{\text{sct}}(\boldsymbol{x}_T, k_2)\,, \tag{20}$$

we arrive at an IE for the electric field in the k_2-domain:

$$\tilde{\boldsymbol{E}}^{\text{inc}}(\boldsymbol{x}_T, k_2) = \tilde{\boldsymbol{E}}(\boldsymbol{x}_T, k_2) - \left(k_0^2 + \tilde{\boldsymbol{\nabla}}\tilde{\boldsymbol{\nabla}}\cdot\right) \tilde{\boldsymbol{A}}(\boldsymbol{x}_T, k_2)\,, \tag{21}$$

where $\tilde{\boldsymbol{A}}(\boldsymbol{x}_T, k_2)$ is given in eq. (10). For each k_2 value, eq. (21) represents an IE from which $\tilde{\boldsymbol{E}}(\boldsymbol{x}_T, k_2)$ can be determined.

We introduce an operator notation and write the IE as follows:

$$\tilde{\boldsymbol{E}}^{\text{inc}} = \tilde{\boldsymbol{E}} - \tilde{\boldsymbol{G}}_D \cdot \left[\chi \tilde{\boldsymbol{E}}\right], \quad \text{on } D\,, \tag{22}$$

where

$$\tilde{\boldsymbol{G}}_D \cdot \tilde{\boldsymbol{w}} = \left(k_0^2 + \tilde{\boldsymbol{\nabla}}\tilde{\boldsymbol{\nabla}}\cdot\right) \int_{\boldsymbol{x}'_T \in D} \tilde{G}(\boldsymbol{x}_T - \boldsymbol{x}'_T, k_2) \tilde{\boldsymbol{w}}(\boldsymbol{x}'_T, k_2)\, dA\,. \tag{23}$$

To solve eq. (22) we minimize a cost function defined by:

$$F(\tilde{\boldsymbol{E}}) = \frac{\sum_{k_2} \beta(k_2) \|\tilde{\boldsymbol{E}}^{\text{inc}} - \tilde{\boldsymbol{E}} + \tilde{\boldsymbol{G}}_D \cdot [\chi \tilde{\boldsymbol{E}}]\|_D^2}{\sum_{k_2} \beta(k_2) \|\tilde{\boldsymbol{E}}^{\text{inc}}\|_D^2}\,, \tag{24}$$

where the L^2-norm on D is given by

$$\|\tilde{\boldsymbol{E}}\|_D^2 = \langle \tilde{\boldsymbol{E}}, \tilde{\boldsymbol{E}} \rangle_D = \int_{\boldsymbol{x}_T \in D} \tilde{\boldsymbol{E}}(\boldsymbol{x}_T, k_2) \cdot \overline{\tilde{\boldsymbol{E}}(\boldsymbol{x}_T, k_2)}\, dA\,, \tag{25}$$

in which the overline denotes the complex conjugate.

A convenient way to minimize this cost function iteratively is to use a CG updating scheme van den Berg (1984) where we update the field as follows:

$$\tilde{\boldsymbol{E}}_n(\boldsymbol{x}_T, k_2) = \tilde{\boldsymbol{E}}_{n-1}(\boldsymbol{x}_T, k_2) + \alpha_n^E \tilde{\boldsymbol{v}}_n(\boldsymbol{x}_T, k_2)\,, \quad n > 1\,, \tag{26}$$

where $\tilde{\boldsymbol{v}}_n$ is a CG direction, while the parameter α_n^E is determined by minimizing eq. (24). The detail expressions of this CG direction can be found in Abubakar & van den Berg (2004). Once $\tilde{\boldsymbol{E}}_n$ in D has been determined, the 1-D spatial Fourier transform of the scattered magnetic field at a number of measurement points $\boldsymbol{x}_T^R$ is determined through

$$\tilde{\boldsymbol{H}}^{\text{sct}}(\boldsymbol{x}_T^R, k_2) = \sigma_0 \int_{\boldsymbol{x}'_T \in D} \tilde{\boldsymbol{\nabla}}^R \times \left[\tilde{G}\left(\boldsymbol{x}_T^R - \boldsymbol{x}'_T, k_2\right) \chi(\boldsymbol{x}'_T) \tilde{\boldsymbol{E}}(\boldsymbol{x}'_T, k_2)\right] dA, \tag{27}$$

for $\boldsymbol{x}_T^R \in S$, where S is the domain including all the measurement points and $\tilde{\boldsymbol{\nabla}} = (\partial_1^R, -\text{i}k_2, \partial_3^R)$. Carrying out the differentiations with respect to x_1^R and x_3^R, the magnetic field components at the measurement points are obtained as

$$\begin{aligned}
\tilde{H}_1^{\text{sct}}(\boldsymbol{x}_T^R, k_2) &= \sigma_0 \int_{\boldsymbol{x}'_T \in D} \left[-\text{i}k_2 \tilde{G}\left(\boldsymbol{x}_T^R - \boldsymbol{x}'_T, k_2\right) \chi(\boldsymbol{x}'_T) \tilde{E}_3(\boldsymbol{x}'_T, k_2) - \partial_3^R \tilde{G}\left(\boldsymbol{x}_T^R - \boldsymbol{x}'_T, k_2\right) \chi(\boldsymbol{x}'_T) \tilde{E}_2(\boldsymbol{x}'_T, k_2)\right] dA,\\
\tilde{H}_2^{\text{sct}}(\boldsymbol{x}_T^R, k_2) &= \sigma_0 \int_{\boldsymbol{x}'_T \in D} \left[-\partial_1^R \tilde{G}\left(\boldsymbol{x}_T^R - \boldsymbol{x}'_T, k_2\right) \chi(\boldsymbol{x}'_T) \tilde{E}_3(\boldsymbol{x}'_T, k_2) + \partial_3^R \tilde{G}\left(\boldsymbol{x}_T^R - \boldsymbol{x}'_T, k_2\right) \chi(\boldsymbol{x}'_T) \tilde{E}_1(\boldsymbol{x}'_T, k_2)\right] \text{dA},\\
\tilde{H}_3^{\text{sct}}(\boldsymbol{x}_T^R, k_2) &= \sigma_0 \int_{\boldsymbol{x}'_T \in D} \left[\partial_1^R \tilde{G}\left(\boldsymbol{x}_T^R - \boldsymbol{x}'_T, k_2\right) \chi(\boldsymbol{x}'_T) \tilde{E}_2(\boldsymbol{x}'_T, k_2) + \text{i}k_2 \tilde{G}\left(\boldsymbol{x}_T^R - \boldsymbol{x}'_T, k_2\right) \chi(\boldsymbol{x}'_T) \tilde{E}_1(\boldsymbol{x}'_T, k_2)\right] dA\,,
\end{aligned} \tag{28}$$

where the derivatives of the Green function, $\partial_1^R \tilde{G}$ and $\partial_3^R \tilde{G}$, directly follow from (17) and (18) upon replacing $\{x_1, x_3\}$ by $\{x_1^R, x_3^R\}$ and $\{x_1^S, x_3^S\}$ by $\{x'_1, x'_3\}$, respectively. To arrive at numerical results, the IE in (22) has to be discretized. The discretization procedure is discussed in Appendix A.

5 SYMMETRY WITH RESPECT TO THE TRANSVERSE PLANE

Since the sources and receivers are located at $x_2 = 0$ and the configuration is symmetric with respect to the plane $x_2 = 0$, the electromagnetic field exhibits some symmetry properties as well, see de Hoop (1995). Dependent on the polarization of the exciting source, the electromagnetic field components are either even or odd with respect to the plane $x_2 = 0$, in particular we have

$$\begin{aligned} &H_1 = \text{even},\ H_2 = \text{odd},\ H_3 = \text{even},\ \boldsymbol{M} = \{1, 0, 0\},\\ &H_1 = \text{odd},\ H_2 = \text{even},\ H_3 = \text{odd},\ \boldsymbol{M} = \{0, 1, 0\},\\ &H_1 = \text{even},\ H_2 = \text{odd},\ H_3 = \text{even},\ \boldsymbol{M} = \{0, 0, 1\}. \end{aligned} \tag{29}$$

Since the odd fields vanish for $x_2 = 0$, we are only interested in the even field components. The latter can be approximated by a summation of the spectral quantities over positive k_2 only. As a consequence, in the computations we restrict ourselves to positive k_2 values. After solving of the forward problem for these positive spectral parameters, the even scattered magnetic field components in the plane $x_2 = 0$ are obtained as, *cf*. (19),

$$\boldsymbol{H}^{\text{sct}}(\boldsymbol{x}_T^R, 0) \approx \sum_{k_2 \geq 0} \beta(k_2) \tilde{\boldsymbol{H}}^{\text{sct}}(\boldsymbol{x}_T, k_2), \tag{30}$$

where $\beta(k_2) = \Delta k_2/\pi$ and the odd components of the scattered magnetic fields are enforced to be zero.

6 FORWARD MODELLING RESULTS

As a test case, we consider a configuration shown in Fig. 1. In this configuration we have two resistive layers with conductivity 0.1 S/m for the top and 0.02 S/m for the bottom. The thicknesses of the top and bottom layers are 30 and 15 m, respectively. Embedded inside the top layer, adjacent to the well located at $x_1 = -25$ m, there is an anomaly with dimension of 30 m by 15 m and with conductivity, that is, $\sigma = 1$ S/m. The background conductivity is $\sigma_0 = 0.2$ S/m. The field is generated by a magnetic point dipole located in the well at $x_1 = -25$ m. The vertical position of the source is $x_3 = 0$. The frequency of operation of the source is 500 Hz. We assume that in another well located at $x_1 = 25$ m the magnetic fields are measured using an array of receivers distributed uniformly from $x_3 = -60$ m to $x_3 = 60$ m. The object domain D is discretized using a square mesh with $\Delta x_1 = \Delta x_3 = \Delta x$ (see Appendix A).

The midpoint points on each sample in the Fourier spectral domain are given by

$$k_{2,q} = \left(q - \frac{1}{2}\right) \Delta k_2\,, \quad q = 1, \ldots, Q\,. \tag{31}$$

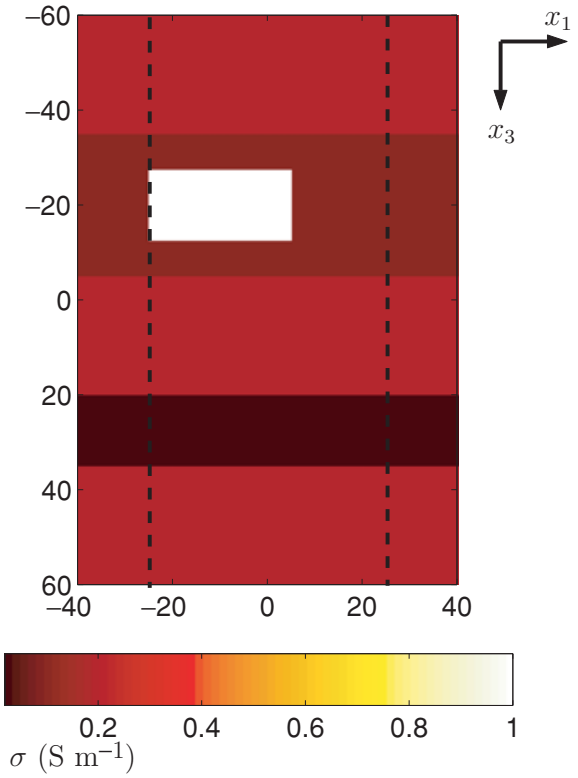

Figure 1. The conductivity distribution of the test configuration. The well-bores are denoted by the dashed lines and are located at $x_1 = -25$ m and $x_1 = 25$ m.

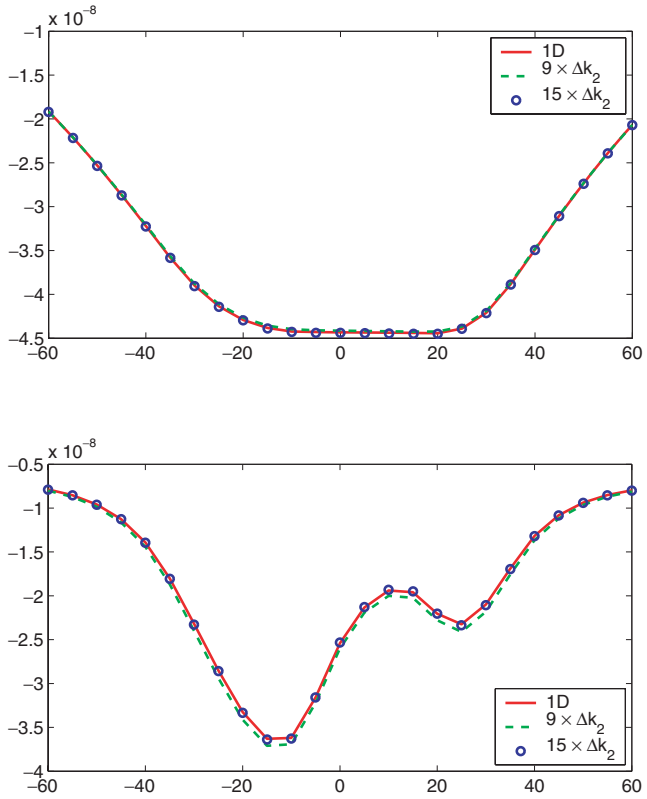

Figure 2. The vertical scattered magnetic field $H_3^{\rm sct}(x_1, x_3)$ at $x_1 = 25$ m as a function of x_3 in a horizontally layered medium; analytical results (*solid lines*) and IE results with 9 k_2-points (*dashed lines*) and 15 k_2-points (*circles*). The domain D has an extent of 320 m in the x_1-direction.

As we previously mentioned, one of the k_2-values should coincide with $k_2 = \mathrm{Re}(k_0) = \delta^{-1}$, where δ is the skin depth of the background medium. For our configurations and frequencies of interest, we found that a sampling distance of $\Delta k_2 = 0.5\,\mathrm{Re}(k_0)$ in the spectral domain is sufficient, as far as computational accuracy and efficiency are concerned. With a minimum skin depth of about 22 m in the configuration, a spatial discretization of the object domain in terms of subsquares with side length of $\Delta x = 2.5$ m is sufficient. Using an equidistant mesh in the spectral domain, the Courant condition prescribes the necessary number, N, of sampling points of the discretized Fourier integral. Hence, $N = (\Delta k_2 \Delta x_2)^{-1} \approx 40$. This number includes the positive and negative samples. Hence, with the use of symmetry, we need at least $Q = 20$ positive sampling points in the spectral domain. A more sophisticated way to determine the optimal spectral Fourier discretization based on the work by Ingerman *et al.* (2000) is currently under investigation.

In order to investigate the accuracy of our 2.5-D IE method we solve it for a horizontally layered medium. This is the configuration of Fig. 1 without the high conductivity anomaly. We compare the IE results with the analytical results of a vertical magnetic dipole in a horizontally layered medium using a code developed by Habashy & Luling (1994).

First, we investigate the dependence of the numerical results on the choice of the spectral parameter k_2. The real and imaginary parts of the complex vertical component of the scattered magnetic field $H_3^{\rm sct}$ are presented in Fig. 2. We observe that the results of our IE approach for $Q = 9$ (dashed lines) show some visible discrepancies with the analytical 1-D results (solid lines) especially in the imaginary part of the scattered magnetic field. Increasing the total number of sample points, we observe that for $Q = 15$ the results (circles) almost coincide with the analytical 1-D results. We conclude that the total sampling length of $(15 - \frac{1}{2})\Delta k_2 = 7.5\,\mathrm{Re}(k_0)$ is satisfactory, and we will use the present spectral discretization throughout this paper.

Secondly, we investigate effect of truncation on the extent of the domain D in the x_1-direction. For computational efficiency, we would like to operate with the smallest domain possible. In Fig. 3, we present the real and imaginary parts of the complex vertical component of the scattered magnetic field for a configuration with two different sizes, 80 m and 320 m. The results for an extent of 80 m (dashed lines) deviate from the analytical results (solid lines) by about 5 per cent whereas, the results for an extent of 320 m (circles) agree very well. In order to save computation time we use in our inversion scheme an extent of 80 m only. We found that an error of 5 per cent does not have significant effect on the inversion results. The discrepancies noted with the exact results are of the order of the noise level, hence, there is no need to take a larger extent in the inversion.

To validate our results for the actual configuration of Fig. 1 including the anomaly, we compare the results of our 2.5-D IE method with the 3-D spectral Lanczos decomposition method (SLDM) developed by Druskin *et al.* (1999), where the length of the object configuration in the transversal direction, x_1 and x_2, is set to 1000 m. Although at first sight the results of both methods agree well (see Fig. 4), we observe some discrepancies. We surmise that these discrepancies are mainly due to the different models of the magnetic dipole source used in the

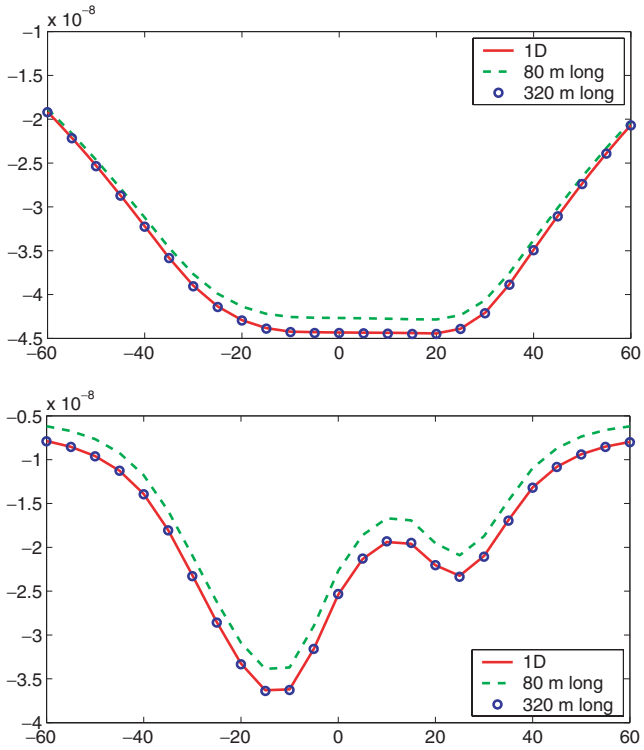

Figure 3. The vertical scattered magnetic field $H_3^{\rm sct}(x_1, x_3)$ at $x_1 = 25$ m as a function of x_3 in a horizontally layered medium; analytical results (*solid lines*) and IE results for a domain D with an extent of 80 m (*dashed lines*) and 320 m (*circles*) in the x_1-direction, respectively.

two forward modelling codes. In the IE method the magnetic dipole source is modelled as a concentrated source in a subsquare, while in the SLDM method, the magnetic dipole is modelled as a square loop over the boundary of a subsquare.

7 INVERSE PROBLEM

In the inverse problem we assume that we collect the data using a number of triaxial sources ($j = 1, 2, \ldots, J$). This numbering includes the different source locations and the three different orientations of the magnetic dipoles sources. For each source of certain orientation at $x_2 = 0$ we measure the electromagnetic field with a number of receivers at $\boldsymbol{x}_T^R \in S$ in the cross-section $x_2 = 0$. With the three measured magnetic-field components, the data equation has the form:

$$\boldsymbol{H}_j^{\rm sct}\big(\boldsymbol{x}_T^R, 0\big) = \sum_{k_2 \geq 0} \beta(k_2) \int_{\boldsymbol{x}'_T \in D} \sigma_0 \tilde{\boldsymbol{\nabla}}^R \times \big[\tilde{G}\big(\boldsymbol{x}_T^R - \boldsymbol{x}'_T, k_2\big) \tilde{\boldsymbol{w}}_j(\boldsymbol{x}'_T, k_2)\big] dA, \qquad \boldsymbol{x}_T^R \in S, \tag{32}$$

where in eq. (32) we have introduced the contrast source defined by,

$$\tilde{\boldsymbol{w}}_j(\boldsymbol{x}_T, k_2) = \chi(\boldsymbol{x}_T) \tilde{\boldsymbol{E}}_j(\boldsymbol{x}_T, k_2). \tag{33}$$

In the 2.5-D configuration under consideration and for each source–receiver spacing, we have five non-zero components of the magnetic field which we represent in the following operator form

$$\boldsymbol{H}_j^{\rm sct} = \sum_{k_2 \geq 0} \beta(k_2)\, \tilde{\boldsymbol{G}}_S \cdot \tilde{\boldsymbol{w}}_j\,, \quad \text{on } S\,. \tag{34}$$

where $\tilde{\boldsymbol{G}}_S \cdot \tilde{\boldsymbol{w}}_j = [\tilde{\boldsymbol{G}}_S \cdot \tilde{\boldsymbol{w}}_j](\boldsymbol{x}_T^R, k_2)$ is given by

$$\tilde{\boldsymbol{G}}_S \cdot \tilde{\boldsymbol{w}}_j = \int_{\boldsymbol{x}'_T \in D} \sigma_0 \tilde{\boldsymbol{\nabla}}^R \times \big[\tilde{G}\,\big(\boldsymbol{x}_T^R - \boldsymbol{x}'_T, k_2\big)\, \tilde{\boldsymbol{w}}_j(\boldsymbol{x}'_T, k_2)\big]\, dA. \tag{35}$$

Eq. (34) is referred to as the data equation. Note that, for each k_2, $\tilde{\boldsymbol{G}}_S$ is an operator mapping $L^2(D)$ into $L^2(S)$. Further we also define the L^2-norm over the data domain S as follows:

$$\big\|\boldsymbol{H}_j^{\rm sct}\big\|_S^2 = \big\langle \boldsymbol{H}_j^{\rm sct}, \boldsymbol{H}_j^{\rm sct} \big\rangle_S = \int_{\boldsymbol{x}_T^R \in S} \boldsymbol{H}_j^{\rm sct}\,\big(\boldsymbol{x}_T^R, 0\big) \cdot \overline{\boldsymbol{H}_j^{\rm sct}\,\big(\boldsymbol{x}_T^R, 0\big)}\, dA\,. \tag{36}$$

Introducing the contrast sources in the IE of eq. (22), we obtain the object equation

$$\chi \tilde{\boldsymbol{E}}_j^{\rm inc} = \tilde{\boldsymbol{w}}_j - \chi \tilde{\boldsymbol{G}}_D \cdot \tilde{\boldsymbol{w}}_j\,, \quad \text{on } D\,, \tag{37}$$

where $\tilde{\boldsymbol{G}}_D \cdot \tilde{\boldsymbol{w}}_j = [\tilde{\boldsymbol{G}}_D \cdot \tilde{\boldsymbol{w}}_j](\boldsymbol{x}_T^R, k_2)$ is given by

$$\tilde{\boldsymbol{G}}_D \cdot \tilde{\boldsymbol{w}}_j = \left(k_0^2 + \tilde{\boldsymbol{\nabla}}\tilde{\boldsymbol{\nabla}}\cdot\right) \int_{\boldsymbol{x}_T' \in D} \tilde{G}(\boldsymbol{x}_T - \boldsymbol{x}_T', k_2)\, \chi(\boldsymbol{x}_T')\, \tilde{\boldsymbol{E}}(\boldsymbol{x}_T', k_2)\, dA\,. \tag{38}$$

For each k_2, $\tilde{\boldsymbol{G}}_D$ is an operator mapping $L^2(D)$ into itself. The inverse scattering problem can be formulated as follows: solving the data equation in eq. (34) to determine the contrast function χ on the object domain D from the knowledge of the incident electric fields $\tilde{\boldsymbol{E}}_j^{\text{inc}}$ on D and the scattered magnetic fields $\boldsymbol{H}_j^{\text{sct}}$ on the data domain S subject to the necessary condition that the contrast sources $\tilde{\boldsymbol{w}}_j$ and the contrast χ satisfy the object equation in (37).

In the CSI method (van den Berg & Kleinman 1997), the inverse scattering problem is formulated as an optimization problem to find the contrast χ and the contrast sources $\tilde{\boldsymbol{w}}_j$. To that end we define the following cost functional:

$$F(\chi, \tilde{\boldsymbol{w}}_j) = F^S(\tilde{\boldsymbol{w}}_j) + F^D(\chi, \tilde{\boldsymbol{w}}_j)\,, \tag{39}$$

where

$$F^S(\tilde{\boldsymbol{w}}_j) = \frac{\sum_j \left\| \boldsymbol{H}_j^{\text{sct}} - \sum_{k_2 \geq 0} \beta(k_2)\, \tilde{\boldsymbol{G}}_S \cdot \tilde{\boldsymbol{w}}_j \right\|_S^2}{\sum_j \left\| \boldsymbol{H}_j^{\text{sct}} \right\|_S^2} \tag{40}$$

and

$$F^D(\chi, \tilde{\boldsymbol{w}}_j) = \frac{\sum_{k_2 \geq 0} \beta(k_2) \sum_j \left\| \chi\, \tilde{\boldsymbol{E}}_j^{\text{inc}} - \tilde{\boldsymbol{w}}_j + \chi\, \tilde{\boldsymbol{G}}_D \cdot \tilde{\boldsymbol{w}}_j \right\|_D^2}{\sum_{k_2 \geq 0} \beta(k_2) \sum_j \left\| \chi\, \tilde{\boldsymbol{E}}_j^{\text{inc}} \right\|_D^2}\,. \tag{41}$$

In each iteration, the contrast sources $\tilde{\boldsymbol{w}}_j$ and the contrast χ are updated alternatingly.

8 UPDATING THE CONTRAST SOURCES

The contrast sources are updated using a CG approach. In the nth iteration, we define the data error to be

$$\boldsymbol{\rho}_{j,n} = \boldsymbol{H}_j^{\text{sct}} - \sum_{k_2 \geq 0} \beta(k_2)\, \tilde{\boldsymbol{G}}_S \cdot \tilde{\boldsymbol{w}}_{j,n}\,, \tag{42}$$

and the object error to be

$$\tilde{\boldsymbol{r}}_{j,n} = \chi_n \tilde{\boldsymbol{E}}_j^{\text{inc}} - \tilde{\boldsymbol{w}}_{j,n} + \chi_n\, \tilde{\boldsymbol{G}}_D \cdot \tilde{\boldsymbol{w}}_{j,n}\,. \tag{43}$$

From the knowledge of the $(n-1)$th iteration, $\tilde{\boldsymbol{w}}_{j,n-1}$ and χ_{n-1}, we update $\tilde{\boldsymbol{w}}_j$ by the following CG step

$$\tilde{\boldsymbol{w}}_{j,n}(\boldsymbol{x}_T, k_2) = \tilde{\boldsymbol{w}}_{j,n-1}(\boldsymbol{x}_T, k_2) + \alpha_n^w \tilde{\boldsymbol{v}}_{j,n}(\boldsymbol{x}_T, k_2), \tag{44}$$

where α_n^w is a constant minimizer and $\tilde{\boldsymbol{v}}_{j,n}$ is an update direction. This update direction is the Polak-Ribière conjugate gradient direction

$$\begin{aligned} &\tilde{\boldsymbol{v}}_{j,0}(\boldsymbol{x}_T, k_2) = \boldsymbol{0}, \\ &\tilde{\boldsymbol{v}}_{j,n}(\boldsymbol{x}_T, k_2) = \tilde{\boldsymbol{g}}_{j,n}(\boldsymbol{x}_T, k_2) + \xi_n \tilde{\boldsymbol{v}}_{j,n-1}(\boldsymbol{x}_T, k_2)\,,\ n \geq 1, \end{aligned} \tag{45}$$

where $\tilde{\boldsymbol{g}}_j$ is the gradient of the cost functional with respect to $\tilde{\boldsymbol{w}}_j$ evaluated at $\tilde{\boldsymbol{w}}_{j,n-1}$ and χ_{n-1}. Explicitly, the gradient for the updating of the contrast source is found to be

$$\tilde{\boldsymbol{g}}_{j,n} = -\eta^S \tilde{\boldsymbol{G}}_S^* \cdot \boldsymbol{\rho}_{j,n-1} - \eta_{n-1}^D \left[\tilde{\boldsymbol{r}}_{j,n-1} - \tilde{\boldsymbol{G}}_D^* \cdot (\chi_{n-1} \tilde{\boldsymbol{r}}_{j,n-1})\right], \tag{46}$$

where the normalization factors are given by

$$\begin{aligned} \eta^S &= \left(\sum_j \left\| \boldsymbol{H}_j^{\text{sct}} \right\|_S^2 \right)^{-1}, \\ \eta_{n-1}^D &= \left(\sum_{k_2 \geq 0} \beta(k_2) \sum_j \left\| \chi_{n-1} \tilde{\boldsymbol{E}}_j^{\text{inc}} \right\|_D^2 \right)^{-1}. \end{aligned} \tag{47}$$

In eq. (46), $\tilde{\boldsymbol{G}}_S^*$ is the adjoint of $\tilde{\boldsymbol{G}}_S$ mapping $L^2(S)$ into $L^2(D, k_2)$ and $\tilde{\boldsymbol{G}}_D^*$ is the adjoint of $\tilde{\boldsymbol{G}}_D$ mapping $L^2(D)$ into itself. The adjoint operator $\tilde{\boldsymbol{G}}_S^* \cdot \boldsymbol{\rho}_{j,n-1} = [\tilde{\boldsymbol{G}}_S^* \cdot \boldsymbol{\rho}_{j,n-1}](\boldsymbol{x}_T, k_2)$ is given by

$$\tilde{\boldsymbol{G}}_S^* \cdot \boldsymbol{\rho}_{j,n-1} = \int_{\boldsymbol{x}_T^R \in S} \overline{\sigma_0 \tilde{\boldsymbol{\nabla}}^R} \times \left[\overline{\tilde{G}(\boldsymbol{x}_T^R - \boldsymbol{x}_T, k_2)} \boldsymbol{\rho}_{j,n-1}(\boldsymbol{x}_T^R) \right] dA\,, \tag{48}$$

while the adjoint operator $\tilde{\boldsymbol{G}}_D^* \cdot \tilde{\boldsymbol{r}}_{j,n-1} = [\tilde{\boldsymbol{G}}_D^* \cdot \tilde{\boldsymbol{r}}_{j,n-1}](\boldsymbol{x}_T, k_2)$ is given by

$$\tilde{\boldsymbol{G}}_D^* \cdot \tilde{\boldsymbol{r}}_{j,n-1} = \int_{\boldsymbol{x}_T' \in D} \overline{\tilde{G}(\boldsymbol{x}_T' - \boldsymbol{x}_T, k_2)} \left(\overline{k_0^2 + \tilde{\boldsymbol{\nabla}}' \tilde{\boldsymbol{\nabla}}' \cdot} \right) \tilde{\boldsymbol{r}}_{j,n-1}(\boldsymbol{x}_T', k_2)\, dA. \tag{49}$$

The parameter ξ_n in the Polak-Ribière direction of (45) is computed from:

$$\xi_n = \frac{\mathrm{Re}\left[\sum_{k_2\geq 0}\beta(k_2)\sum_j \langle \tilde{\boldsymbol{g}}_{j,n}, \tilde{\boldsymbol{g}}_{j,n}-\tilde{\boldsymbol{g}}_{j,n-1}\rangle_D\right]}{\sum_{k_2\geq 0}\beta(k_2)\sum_j \|\tilde{\boldsymbol{g}}_{j,n-1}\|_D^2}. \tag{50}$$

With the update directions completely specified, the real parameter α_n^w in eq. (44) is determined to minimize the cost functional

$$\begin{aligned} F_n &= \eta^S \sum_j \left\| \boldsymbol{H}_j^{\mathrm{sct}} - \sum_{k_2\geq 0}\beta(k_2)\tilde{\boldsymbol{G}}_S\cdot\tilde{\boldsymbol{w}}_{j,n}\right\|_S^2 + \eta_{n-1}^D \sum_{k_2\geq 0}\beta(k_2)\sum_j \left\|\chi_{n-1}\tilde{\boldsymbol{E}}_j^{\mathrm{inc}} - \tilde{\boldsymbol{w}}_{j,n} + \chi_{n-1}\tilde{\boldsymbol{G}}_D\cdot\tilde{\boldsymbol{w}}_{j,n}\right\|_D^2 \\ &= \eta^S \sum_j \left\| \boldsymbol{\rho}_{j,n-1} - \alpha_n^w\left(\sum_{k_2\geq 0}\beta(k_2)\tilde{\boldsymbol{G}}_S\cdot\tilde{\boldsymbol{v}}_{j,n}\right)\right\|_S^2 + \eta_{n-1}^D \sum_{k_2\geq 0}\beta(k_2)\sum_j \left\|\tilde{\boldsymbol{r}}_{j,n-1} - \alpha_n^w(\tilde{\boldsymbol{v}}_{j,n} - \chi_{n-1}\tilde{\boldsymbol{G}}_D\cdot\tilde{\boldsymbol{v}}_{j,n})\right\|_D^2, \end{aligned} \tag{51}$$

and it is found explicitly to be

$$\begin{aligned} \alpha_n^w = \mathrm{Re}\Bigg\{ &\eta^S \sum_j \left\langle \boldsymbol{\rho}_{n-1}, \sum_{k_2\geq 0}\beta(k_2)\tilde{\boldsymbol{G}}_S\cdot\tilde{\boldsymbol{v}}_{j,n}\right\rangle_S + \eta_{n-1}^D \sum_{k_2\geq 0}\beta(k_2)\sum_j \langle \tilde{\boldsymbol{r}}_{n-1}, \tilde{\boldsymbol{h}}_{j,n}\rangle_D \Bigg\} \\ &\times \left\{ \eta^S \sum_j \left\| \sum_{k_2\geq 0}\beta(k_2)\tilde{\boldsymbol{G}}_S\cdot\tilde{\boldsymbol{v}}_{j,n}\right\|_S^2 + \eta_{n-1}^D \sum_{k_2\geq 0}\beta(k_2)\sum_j \|\tilde{\boldsymbol{h}}_{j,n}\|_D^2\right\}^{-1}, \end{aligned} \tag{52}$$

with

$$\tilde{\boldsymbol{h}}_{j,n} = \tilde{\boldsymbol{v}}_{j,n} - \chi_{n-1}\tilde{\boldsymbol{G}}_D\cdot\tilde{\boldsymbol{v}}_{j,n}. \tag{53}$$

At this stage, all quantities that are needed to update the contrast sources are known and $\tilde{\boldsymbol{w}}_{j,n}$ can be then calculated. The starting values for $\tilde{\boldsymbol{w}}_{j,n}$ must still be chosen. Unless stated otherwise, as starting values, we choose the contrast sources that minimize the data error, which are the contrast sources obtained by back projection,

$$\tilde{\boldsymbol{w}}_{j,0} = \frac{\sum_{k_2\geq 0}\beta(k_2)\sum_l \|\tilde{\boldsymbol{G}}_S^*\cdot\boldsymbol{H}_l^{\mathrm{sct}}\|_D^2}{\sum_l \left\|\sum_{k_2\geq 0}\beta(k_2)\tilde{\boldsymbol{G}}_S\cdot\left(\tilde{\boldsymbol{G}}_S^*\cdot\boldsymbol{H}_l^{\mathrm{sct}}\right)\right\|_D^2}\,\tilde{\boldsymbol{G}}_S^*\cdot\boldsymbol{H}_j^{\mathrm{sct}}. \tag{54}$$

9 UPDATING THE CONTRAST

We first determine the corresponding total field quantity $\tilde{\boldsymbol{E}}_{j,n} = \tilde{\boldsymbol{E}}_{j,n}(\boldsymbol{x}_T, k_2)$ for a given contrast source $\tilde{\boldsymbol{w}}_{j,n}$ as follows:

$$\tilde{\boldsymbol{E}}_{j,n} = \tilde{\boldsymbol{E}}_j^{\mathrm{inc}} + \tilde{\boldsymbol{G}}_D\cdot\tilde{\boldsymbol{w}}_{j,n}. \tag{55}$$

Then the contrast $\chi_n = \chi_n(\boldsymbol{x}_T)$ is obtained by the minimization of the numerator of the second term of the right-hand side of eq. (39), that is,

$$\chi_n = \min_\chi \left\{ \eta_{n-1}^D \sum_{k_2\geq 0}\beta(k_2)\sum_j \|\chi\tilde{\boldsymbol{E}}_{j,n} - \tilde{\boldsymbol{w}}_{j,n}\|_D^2\right\}. \tag{56}$$

This norm is minimized when

$$\chi_n = \mathrm{Re}\left\{\frac{\sum_{k_2\geq 0}\beta(k_2)\sum_j \tilde{\boldsymbol{w}}_{j,n}\cdot\overline{\tilde{\boldsymbol{E}}_{j,n}}}{\sum_{k_2\geq 0}\beta(k_2)\sum_j |\tilde{\boldsymbol{E}}_{j,n}|^2}\right\}. \tag{57}$$

Note that the update for the contrast is carried out by an explicit minimization. This procedure has circumvented somehow the ill-posed nature of the inverse problem. In the next section, we discuss the multiplicative regularization to limit large variations in the reconstructed contrast.

10 MULTIPLICATIVE REGULARIZATION

It has been shown that the quality of the reconstruction for the CSI method will improve substantially by employing a multiplicative regularization technique (Abubakar *et al.* 2003; Abubakar & van den Berg 2004). In this MR-CSI method the contrast is found from the extended cost functional defined as follows:

$$C_n(\chi, \tilde{\boldsymbol{w}}_{j,n}) = F_n(\chi, \tilde{\boldsymbol{w}}_{j,n})\, F_n^R(\chi), \tag{58}$$

where the multiplicative regularization factor F_n^R is a weighted L^2-norm, namely,

$$F_n^R(\chi) = \frac{1}{\int_{\boldsymbol{x}_T\in D} dA}\int_{\boldsymbol{x}_T\in D}\frac{|\nabla\chi(\boldsymbol{x}_T)|^2 + \delta_n^2}{|\nabla\chi_{n-1}(\boldsymbol{x}_T)|^2 + \delta_{n-1}^2}\, dA, \tag{59}$$

in which the positive parameter,

$$\delta_n^2 = F_n^D(\chi_{n-1}, \tilde{\boldsymbol{w}}_{j,n},)(\Delta x)^{-2}\,, \tag{60}$$

decreases as the iterations proceeds. We note that $|\nabla\chi|^2 = |\partial_1\chi|^2 + |\partial_3\chi|^2$ is now the variation of the contrast in the transverse plane. A stronger regularization can be obtained with the Cartesian definition of the weighted L_2-norm regularization factor,

$$\begin{aligned} F_n^R(\chi) &= \frac{1}{2\int_{\boldsymbol{x}_T\in D} dA}\int_{\boldsymbol{x}_T\in D}\left[\frac{|\partial_1\chi(\boldsymbol{x}_T)|^2+\delta_n^2}{|\partial_1\chi_{n-1}(\boldsymbol{x}_T)|^2+\delta_{n-1}^2}+\frac{|\partial_3\chi(\boldsymbol{x}_T)|^2+\delta_n^2}{|\partial_3\chi_{n-1}(\boldsymbol{x}_T)|^2+\delta_{n-1}^2}\right]dA \\ &= \|b_{1,n}\boldsymbol{\nabla}\chi\|_D^2+\delta_n^2\|b_{1,n}\|_D^2+\|b_{3,n}\boldsymbol{\nabla}\chi\|_D^2+\delta_n^2\|b_{3,n}\|_D^2, \end{aligned} \tag{61}$$

where

$$b_{1,n} = \left[2\left(\int_{\boldsymbol{x}_T\in D} dA\right)\left(|\partial_1\chi_{n-1}|^2+\delta_{n-1}^2\right)\right]^{-1/2}\,, \tag{62}$$

$$b_{3,n} = \left[2\left(\int_{\boldsymbol{x}_T\in D} dA\right)\left(|\partial_3\chi_{n-1}|^2+\delta_{n-1}^2\right)\right]^{-1/2}\,. \tag{63}$$

Note that when the so-called steering parameter δ_n^2 is very large, the regularization factor is equal to one, and in this case no regularization takes place. On the other hand, when the steering parameter is small, the regularization is effect. With our choice of eq. (60) we have a large steering parameter at the beginning of the optimization process when the data misfit is large and a decreasing one as the iteration proceeds since the data misfit is decreasing.

The contrast will now be updated by finding the minimizer of the full cost functional given in eq. (61). Starting from the update for the contrast in eq. (57) we make an additional minimization step as follows:

$$\chi_n^R = \chi_n + \alpha_n^\chi\, d_n\,. \tag{64}$$

The search direction d_n is given by the Polak-Ribière conjugate gradient and is given by

$$d_0 = 0\,,\ d_n = g_n^R + \frac{\mathrm{Re}\left\langle g_n^R, g_n^R - g_{n-1}^R\right\rangle_D}{\left\|g_{n-1}^R\right\|_D^2}\, d_{n-1}, \quad n>1. \tag{65}$$

We take

$$g_n^R = \frac{\left[\frac{\partial F_n^D(\chi,\tilde{\boldsymbol{w}}_{j,n})}{\partial\chi}\, F_n^R(\chi) + F_n(\chi,\tilde{\boldsymbol{w}}_{j,n})\frac{\partial F_n^R(\chi)}{\partial\chi}\right]_{\chi=\chi_n}}{\sum_{k_2}\beta(k_2)\sum_j|\boldsymbol{E}_{j,n}|^2} = F_n(\chi_n,\tilde{\boldsymbol{w}}_{j,n})\,\frac{\partial_1\cdot\left(b_{1,n}^2\partial_1\chi_n\right)+\partial_2\cdot\left(b_{2,n}^2\partial_2\chi_n\right)}{\sum_{k_2}\beta(k_2)\sum_j|\boldsymbol{E}_{j,n}|^2} \tag{66}$$

being a preconditioned gradient of the cost functional $C_n(\chi,\tilde{\boldsymbol{w}}_{j,n})$ with respect to changes in the contrast around the point $\chi=\chi_n$. Note that there is no contribution from the gradient of F_n^D since around $\chi=\chi_n$ the corresponding gradient has vanished.

This procedure of updating the contrast enables us to find the update parameter α_n^χ in a closed form, provided that α_n^χ is assumed to be a real quantity. Another advantage is that we are able to show that the cost function is a convex function of this real parameter (Abubakar *et al.* 2003). The real parameter α_n^χ is found from a line minimization of the cost functional in eq. (58),

$$\alpha_n^\chi = \min_{\mathrm{real}}\alpha^\chi\left\{F_n\left(\chi_n+\alpha^\chi d_n,\tilde{\boldsymbol{w}}_{j,n}\right)F_n^R\left(\chi_n+\alpha^\chi d_n\right)\right\}. \tag{67}$$

This minimization of a fourth-degree polynomial in α^χ can be performed analytically Press *et al.* (1992),

$$F_n(\alpha^\chi) = [A+B\,(\alpha^\chi)^2][X+2Y\alpha^\chi+Z\,(\alpha^\chi)^2]\,, \tag{68}$$

where

$$X = \|b_{1,n}\partial_1\chi_n\|_D^2+\delta_n^2\|b_{1,n}\|_D^2+\|b_{2,n}\partial_2\chi_n\|_D^2+\delta_n^2\|b_{2,n}\|_D^2\,, \tag{69}$$

$$Y = \mathrm{Re}\langle b_{1,n}\partial_1\chi_n, b_{1,n}\partial_1 d_n\rangle_D + \mathrm{Re}\langle b_{2,n}\partial_2\chi_n, b_{2,n}\partial_2 d_n\rangle_D, \tag{70}$$

$$Z = \|b_{1,n}\partial_1 d_n\|_D^2+\|b_{2,n}\partial_2 d_n\|_D^2, \tag{71}$$

$$A = F_n(\chi_n,\tilde{\boldsymbol{w}}_{j,n})\,, \tag{72}$$

$$B = \eta_{n-1}^D\sum_{k_2}\beta(k_2)\sum_j\|d_n\tilde{\boldsymbol{E}}_{j,n}\|_D^2\,. \tag{73}$$

11 RECIPROCITY BASED COMPLETION OF DATA

In many practical situations we can generate extra data set using the principle of source/receiver reciprocity de Hoop (1995). For example, in the cross-well logging problem, the sources are located in the first well, while the receivers are located in the second one. Using reciprocity we

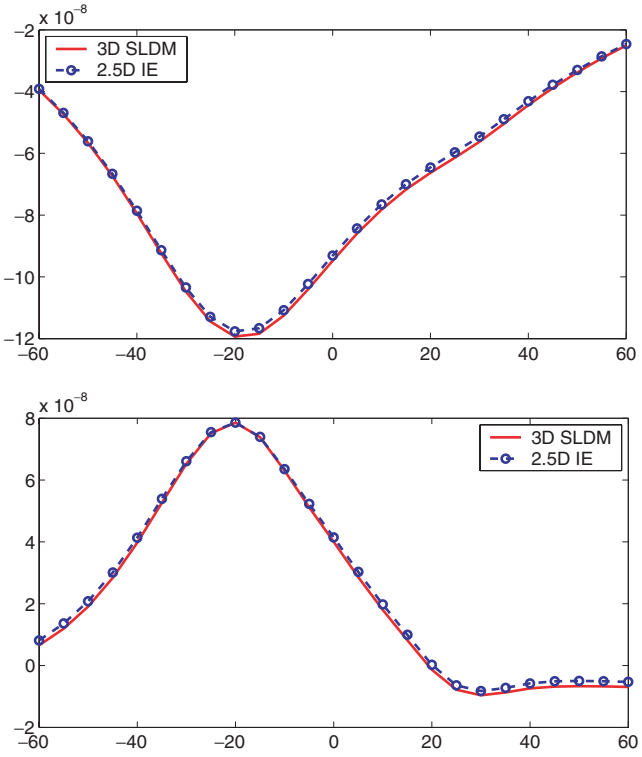

Figure 4. The vertical scattered magnetic field component $H_3(x_1, x_3)$ at $x_1 = 25$ m as a function of x_3 in the configuration of Fig. 1; results of the 3-D SLDM method for an object of 320-m-long (*solid lines*), 2.5-D IE results (*dashed lines marked by circles*).

may interchange each source/receiver pair. In this way we are able to construct extra field data generated by a source in the second well and measured by receivers in the first well. Obviously, such extra data are redundant, however, incorporating this extra data, helps in symmetrizing the sensitivity of inversion around the transmitter and receiver wells.

12 INVERSION RESULTS

As an example we consider the configuration shown in Fig. 1. This example is a representative configuration of monitoring fluid movement in a reservoir. The data used in the inversion is assumed to be triaxial data. For each source–receiver pair we have nine components of the magnetic fields. However, note that since the configuration is 2-D, only five components of the magnetic field are non-zeros. These components are H_{11}, H_{13}, H_{22}, H_{31} and H_{33} where the first subscript denotes the source orientation while the second subscript denotes the receiver orientation. The synthetic data sets for the inversion experiments are generated by solving the forward problem numerically using the 3-D SLDM code Druskin *et al.* (1999). After generation of these data sets we added a 5 per cent random white noise according to:

$$\boldsymbol{H}_j^{\text{sct, noise}} = 0.05\,[1 + (\phi_j + \mathrm{i}\,\psi_j)]\boldsymbol{H}_j^{\text{sct}}, \quad j = 1, \ldots, \tag{74}$$

where ϕ_j and ψ_j are different random numbers for each j varying from -1 to $+1$. In order to measure the quality of the inverted conductivity distribution, we define the error in the reconstructed conductivity as follows:

$$\text{ERR}_n = \frac{1}{\int_{\boldsymbol{x}_T \in D} dA} \int_{\boldsymbol{x}_T \in D} \left| \frac{\sigma_n(\boldsymbol{x}_T) - \sigma^{\text{true}}(\boldsymbol{x}_T)}{\sigma^{\text{true}}(\boldsymbol{x}_T)} \right| dA, \tag{75}$$

where $\sigma_n(\boldsymbol{x}_T)$ is the reconstructed conductivity distribution at the nth iteration and σ^{exact} is the true conductivity distribution. We will consider inversion using the cross-well, single-well and joint cross-well-single-well data.

12.1 Cross-well data inversion

In the cross-well inversion experiment we have 29 sources located uniformly at the left well-bore ($x_1 = -25$ m) from $x_3 = -70$ m up to $x_3 = 70$ m. For each source we measured the data using 30 receivers located at right well-bore ($x_1 = 25$ m) from $x_3 = -72.5$ m up to $x_3 = 72.5$ m. These source and receiver wells are denoted by the dashed lines in Fig. 1. The frequency operation of the sources is 500 Hz. The employed cross-well measurement system is very similar to the one used by Wilt *et al.* (1995).

The inversion domain D has dimensions of 80 m in the x_1-direction and 120 m in the x_3-direction. This domain is subdivided into 32×48 subsquares. This discretization of 2.5 m represents about 5 per cent of the well spacing, which is expected to be the resolution of our

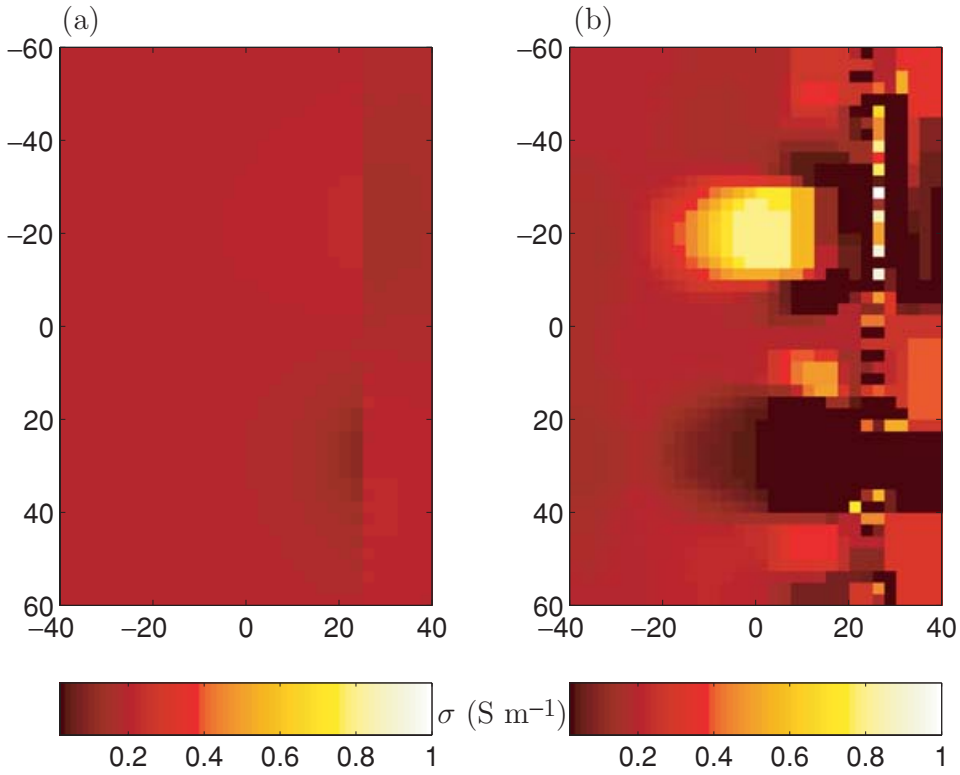

Figure 5. The conductivity σ (S/m) distribution of the back-propagation (a) and the full inversion (b) from cross-well data without invoking reciprocity.

measurement system. First we carry out an inversion without using the reciprocity approach described in the previous section. In this case the total number of data points is equal to $5 \times 29 \times 30$. The results of the back-propagation step are given in Fig. 5(a) and the results of the full inversion process after 1024 iterations are given in Fig. 5(b). The relative error in the reconstructed conductivity after the back-propagation step and the full non-linear inversion step amounts to $\mathrm{ERR}_0 = 1.307$ and $\mathrm{ERR}_{1024} = 1.020$, respectively.

Next in order to improve the inversion results we use the reciprocity principle. As a result of this process, the number of data points is doubled. The back-propagation and the inversion results from this set of data are given in Figs 6(a) and (b). The relative error in the conductivity after 1024 iterations now amounts to 0.371. We observe that by using the reciprocity principle we can significantly improve the reconstruction results. However, this technique nearly doubles the computational time. In all of the next cross-well inversion results, reciprocity will be invoked.

12.2 Single-well data inversion

We consider the inversion of the configuration shown in Fig. 1, however, the data is now collected using triaxial single-well measurements. In the tool configuration, we have one triaxial source and two triaxial receivers. The distances between the source and receivers are 2 and 5 m. Hence at each logging point we have 5×2 complex-valued data points.

The data set is collected in the well located at $x_1 = -25$ m using 25 logging points distributed uniformly from $x_3 = -60$ m up to $x_3 = 60$ m. The back-propagation and the full inversion results using this one-side single-well data set are given in Figs 7(a) and (b), respectively. The relative error in the reconstructed conductivity at the end of the optimization process is equal to 0.666. We observe that the inverted conductivity distribution has a good resolution near the well-bore. However, the resolution of the inverted conductivity distribution in the region beyond 15 m (approximately equal to one-third the skin depth in the background medium) from the well-bore degrades significantly.

Further, in Figs 8(a) and (b) we show the back-propagation and the full inversion results using the single-well data set collected at the two wells. The wells are located at $x_1 = -25$ m and $x_1 = 25$ m. In each well we have 25 logging points. In this case the total complex-valued data points equal to $5 \times 50 \times 2$. In Fig. 8(b) we now obtain a good resolution in the inverted conductivity distribution around the well located at $x = 25$ m. The relative error in the reconstructed conductivity is equal to $\mathrm{ERR}_{1024} = 0.287$.

12.3 Joint single-well and cross-well data inversion

In this subsection we consider the inversion of both single-well and cross-well data. This joint inversion is carried out either sequentially or simultaneously.

In the sequential joint inversion we first invert the single-well data using the 1-D version of the inversion algorithm presented in this paper. The results of this 1-D inversion are given in Fig. 9(a) using the one side single-well data set. The relative error in the reconstructed

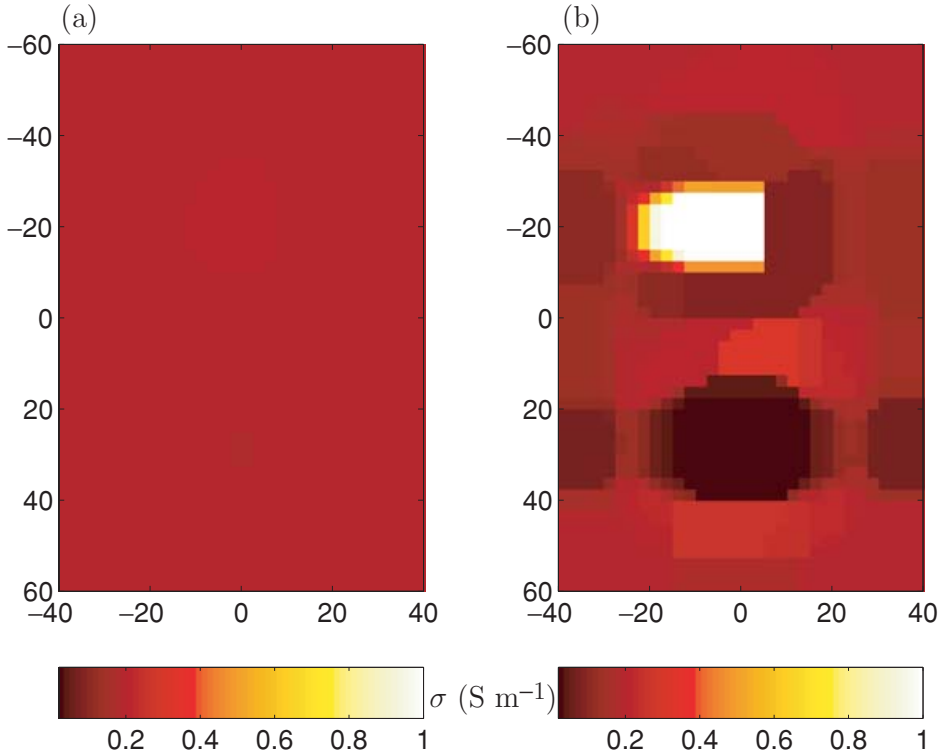

Figure 6. The conductivity σ distribution of the back-propagation (a) and the full inversion (b) from cross-well data invoking reciprocity.

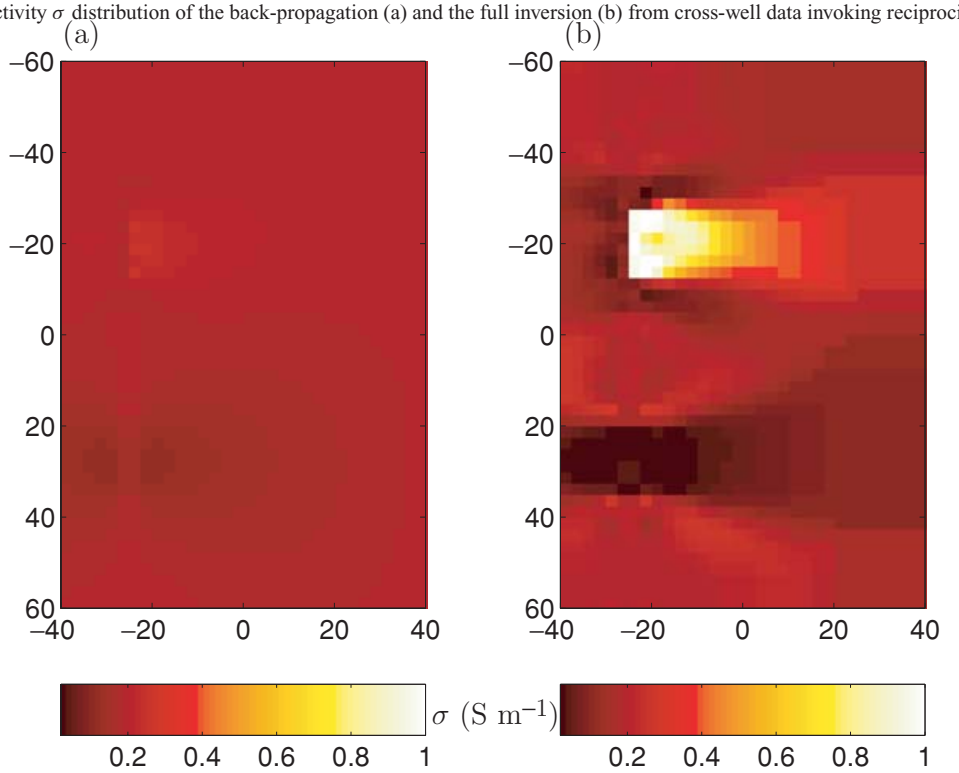

Figure 7. The conductivity σ distribution of the back-propagation (a) and the full inversion (b) from single-well data collected at $x_1 = -25$ m.

conductivity due to this 1-D inversion is 0.335. Note that although the value and the location of the conductivity of the bottom layer is reconstructed very well, the value of the conductivity of the top layer is way overestimated. In the next step, we use this inversion result as the initial estimate for inverting the cross-well data set. Note that in this second step we also use the reciprocity data set. The inversion result is given in Fig. 9(b) and the corresponding relative conductivity error amounts to $\mathrm{ERR}_{1024} = 0.100$.

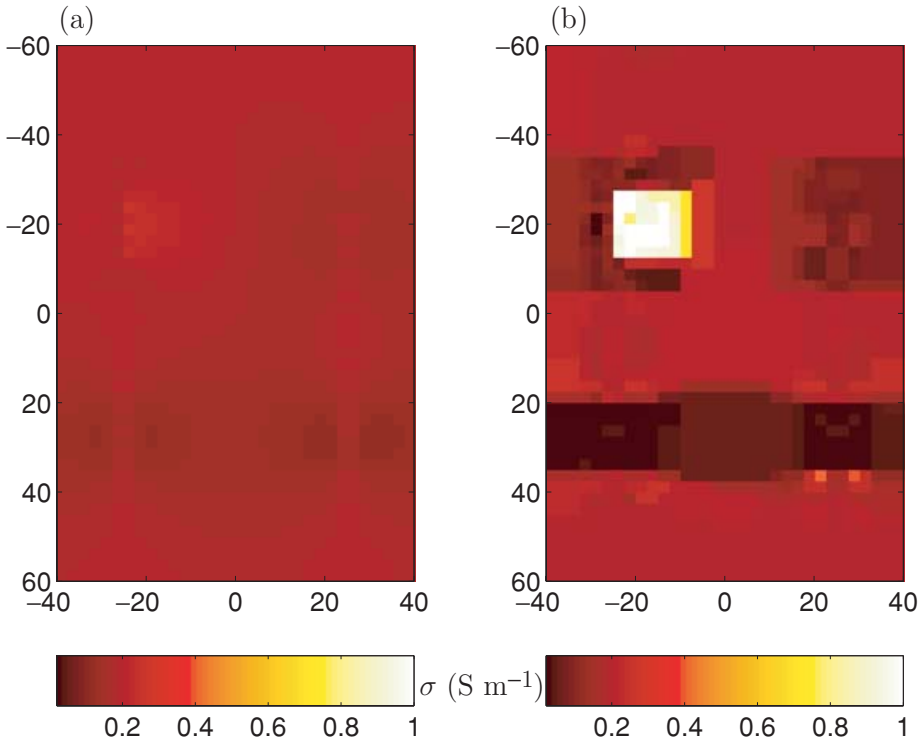

Figure 8. The conductivity σ distribution of the back-propagation (a) and the full inversion (b) from single-well data collected at $x_1 = -25$ m and $x_1 = 25$ m.

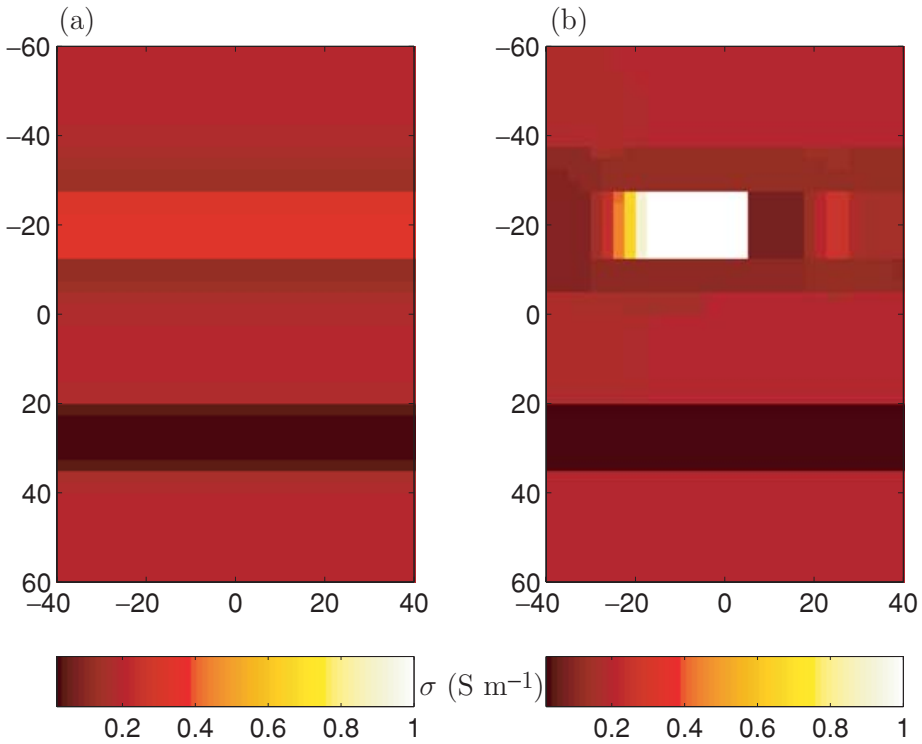

Figure 9. The conductivity σ distribution of the initial estimate (a) obtained with 1-D inversion of single-well data collected at $x_1 = -25$ m and the full inversion result (b) obtained from cross-well data invoking reciprocity.

In Fig. 10 we repeat the same inversion of the previous example, however, with an initial estimate obtained from the single-well data collected at both wells (at $x_1 = -25$ m and $x_1 = 25$ m). The results of this 1-D inversion is given in Fig. 10(a). The corresponding relative error in the reconstructed conductivity is 0.246. Unlike the 1-D results given in Fig. 9(a), the value of the conductivity of the top layer in Fig. 10(a) is slightly below the value of the background conductivity ($\sigma_0 = 0.2$ S/m). The final inversion results using this initial estimate are given in Fig. 10(b). The relative error in the reconstructed conductivity after 1024 iterations is 0.117.

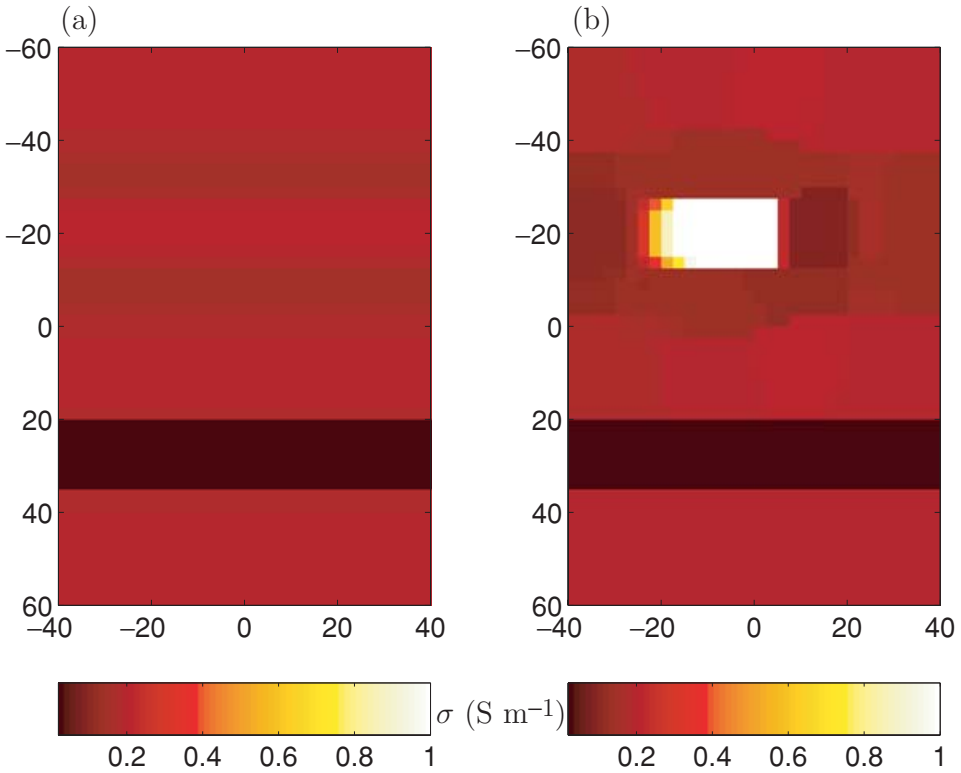

Figure 10. The conductivity σ distribution of the initial estimate (a) obtained with 1-D inversion of single-well data collected at $x_1 = -25$ and $x_1 = 25$ m and the full inversion result (b) obtain from cross-well data invoking reciprocity.

In Fig. 11 we present the results when inverting both single-well and cross-well data sets simultaneously. The corresponding cost functional for carrying out this joint inversion is given by

$$C_n(\chi, \tilde{\boldsymbol{w}}_j^c, \tilde{\boldsymbol{w}}_j^s) = \left[F_n^s(\chi, \tilde{\boldsymbol{w}}_j^s) + F_n^c(\chi, \tilde{\boldsymbol{w}}_j^c)\right] F_n^R(\chi), \tag{76}$$

where $F_n^s(\chi, \tilde{\boldsymbol{w}}_j^s)$ and $F_n^c(\chi, \tilde{\boldsymbol{w}}_j^c)$ are the cost functionals with respect to the single-well and cross-well data, respectively. In each iteration of the optimization step, we first update the contrast sources $\tilde{\boldsymbol{w}}_j^s$ and $\tilde{\boldsymbol{w}}_j^c$ and then the contrast χ. The results after the full non-linear inversion are given in Fig. 11(b). The relative error in the reconstructed conductivity after 1024 iterations is 0.091. This experiment shows that it is advantageous to start the inversion process with an initial estimate where some *a priori* information is taken into account.

Finally we remark that the typical total computational time of the algorithm is about 1–2 hr to invert one data set on a personal computer with a Pentium IV 3.02 GHz processor and 2 GB memory.

13 CONCLUSIONS

In this paper we presented forward and inverse algorithms based on the IE method for solving 2.5-D low-frequency electromagnetic geophysical problems.

In the forward problem, by using a Fourier transformation in the invariant direction of the configuration, the 3-D scattering problem can be reduced to the problem of solving a number of 2-D IEs over the domain of the scatterers. Since we are only interested in the fields in the plane where the sources and receivers are located, the number of Fourier parameters needed to accurately calculate those fields are significantly small. We employ the CGNR method to solve this linear system of equations. By using the CGNR method the convergence of our forward solver is guaranteed for any scatterer and for any frequency of operation. To obtain a positive definite matrix we multiply the original matrix by its adjoint, hence squaring the condition number of the inversion kernel leading to a slow convergence of the method in some cases. Another type of solvers such as the bi-conjugate gradient stabilized (BICGSTAB) by van der Vorst (1992) or the Generalized Minimal Residual (GMRES) by Saad & Schlutz (1986) can be employed to speed up the convergence. However, this investigation is beyond the scope of the paper. After the fields inside the scattering domain are obtained for a number of spatial frequency components, the inverse Fourier transformation is carried out to obtain the fields at the points of observation.

In the inverse problem we employed the MR-CSI method. The advantages of using this particular algorithm are:

(1) There is no full forward problem solved at each step of the optimization process. This allows us to address large-scale inverse problems.

(2) It employs a multiplicative regularization technique. Hence the weighting for the regularization term is determined automatically by the optimization process itself.

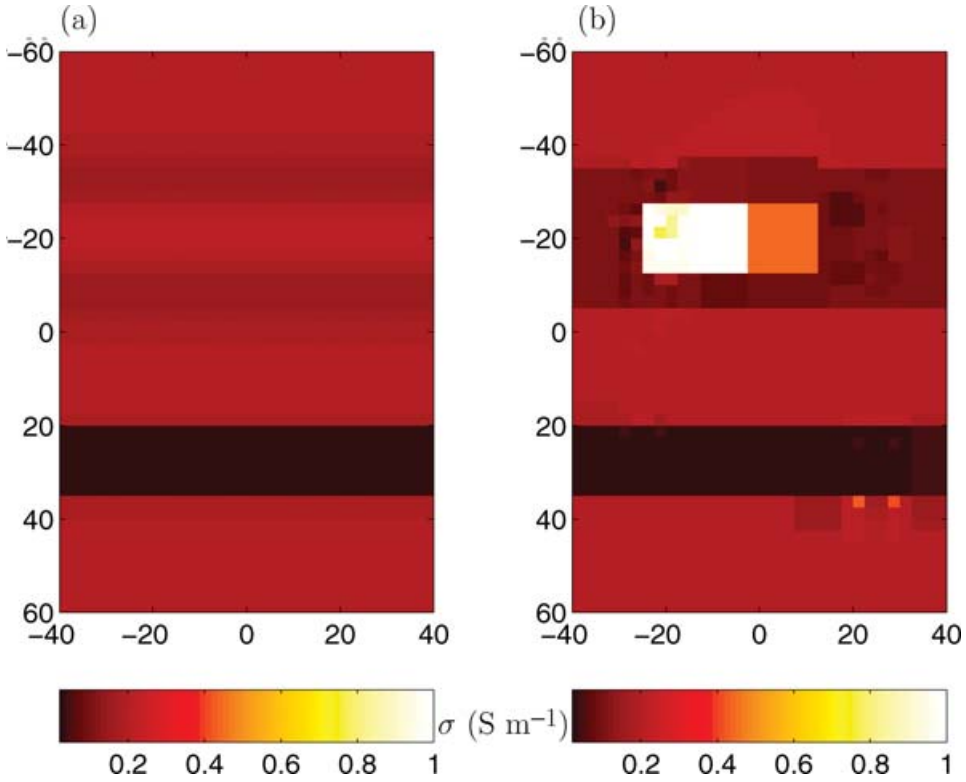

Figure 11. The conductivity σ distribution of the initial estimate (a) obtained with 1-D inversion of single-well data collected at $x_1 = -25$ and $x_1 = 25$ m and the full inversion (b) from cross- and single-well data collected at $x_1 = -25$ m and $x_1 = 25$ m.

(3) It uses a weighted L^2-norm regularizer. This regularizer has all the advantages of the well-known total variation regularizer by Vogel (2002). We presented inversion from the cross-well and long-offset single-well low-frequency electromagnetic geophysical measurements. In the cross-well inversion the advantage of using the source–receiver reciprocity principle was demonstrated. Some advantages of using joint inversion of cross-well and single-well data either sequentially or simultaneously are also shown.

Finally we remark that the extension of the presented inversion algorithm for multifrequency data is rather straightforward, see Bloemenkamp *et al.* (2001).

ACKNOWLEDGMENTS

The authors would like to thank Vladimir Druskin of Schlumberger-Doll Research, Ridgefield, CT, USA and Leonid Knizhnerman of the Central Geophysical Expedition, Moscow, Russia for providing us with their 3-D SLDM code for benchmarking purposes and generating independent synthetic data.

REFERENCES

Abubakar, A. & van den Berg, P.M., 2000. Three-dimensional inverse scattering applied to cross-well induction sensors, *IEEE Transactions on Geoscience and Remote Sensing,* **38,** 1669–1681.

Abubakar, A., van den Berg, P.M. & Semenov, S.Y., 2003. Two- and three-dimensional algorithms for microwave imaging and inverse scattering, *Journal of Electromagnetic Waves and Applications,* **17,** 209–231.

Abubakar, A. & van den Berg, P.M., 2004. Iterative forward and inverse algorithms based on domain integral equations for three-dimensional electric and magnetic objects, *Journal of Computational Physics,* **195,** 236–262.

Allers, A., Sezginer, A. & Druskin, V.L., 1994. Solution of 2.5-dimensional problems using the Lanczos decomposition, *Radio Science,* **29,** 955–963.

Abramowitz, M. & Stegun, I.A., 1968. *Handbook of Mathematical Functions*, Dover Publications, New York.

Alumbaugh, D.L. & Newman, G.A., 1997. 3-D massively parallel electromagnetic inversion; part b—analysis of cross well EM experiment, *Geophysical Journal International,* **128,** 355–363.

Alumbaugh, D.L. & Wilt, M.J., 2001. A numerical sensitivity study of three-dimensional imaging from a single borehole, *Petrophysics,* **42,** 19–31.

Bloemenkamp, R.F., Abubakar, A. & van den Berg, P.M., 2001. Inversion of experimental multi-frequency data using the contrast source inversion method, *Inverse Problems,* **17,** 1611–1622.

de Hoop, A.T., 1995. *Handbook of Radiation and Scattering of Waves*, Academic Press, London.

Druskin, V.L. & Knizhnerman, L.A., 1994. Spectral approach to solving three-dimensional Maxwell's diffusion equations in the time and frequency domain, *Radio Science,* **29,** 937–953.

Druskin, V.L., Knizhnerman, L.A. & Lee, P., 1999. New spectral Lanczos decomposition method for induction modeling in arbitrary 3-D geometry, *Geophysics,* **64,** 701–706.

Habashy, T.M., Chow, E.Y. & Dudley, D.G., 1990. Profile inversion using the renormalized source-type integral equation approach, *IEEE Transactions on Antennas and Propagation,* **38,** 668–682.

Habashy, T.M., Oristaglio, M.L. & de Hoop, A.T., 1994. Simultaneous nonlinear reconstruction of two-dimensional permittivity and conductivity,

Radio Science, **29,** 1101–1118.
Habashy, T.M. & Lulling, M., 1994. *A point magnetic dipole radiator in a layered TI-anisotropic medium*, Technical Report, Schlumberger-Doll Research, Ridgefield, Connecticut, USA.
Ingerman, D., Druskin, V.L. & Knizhnerman, L.A., 2000. Optimal finite difference grids and rational approximations of the square root I. Elliptic problems, *Communications on Pure and Applied Mathematics,* **LIII,** 1039–1066.
Press, W.H., Teukolsky, S.A., Vetterling, W.T. & Flannery, B.P., 1992. *Numerical Recipes in Fortran: The Art of Scientific Computing*, Cambridge University Press, New York.
Richmond, J.H., 1965. Scattering by a dielectric cylinder of arbitary cross section shape, *IEEE Transactions on Antennas and Propagation,* **13,** 334–341.
Saad, Y. & Schultz, M.N., 1986. GMRES: A generalized minimal residual algorithm for solving nonsymmetric linear system, *SIAM J. Aci. Stat. Comp.,* **7,** 856–859.
Spies, B.R. & Habashy, T.M., 1995. Sensitivity analysis of crosswell electromagnetics, *Geophysics,* **60,** 834–845.
Torres-Verdin, C. & Habashy, T.M., 1994. Rapid 2.5-dimensional forward modeling & inversion via a new nonlinear scattering approximation, *Radio Science,* **29,** 1051–1079.
van Bladel, J., 1991. *Singular Electromagnetic Fields and Sources*, Clarendon, Oxford.
van den Berg, P.M., 1984. Iterative computational techniques in scattering based upon the integrated square error criterion, *IEEE Transactions on Antennas and Propagation,* **32,** 1063–1071.
van den Berg, P.M. & Kleinman, R.E., 1997. A contrast source inversion method, *Inverse Problems,* **13,** 1607–1620.
van der Vorst, H.A., 1992. BICGSTAB: A fast & smoothly convergence variant of Bi-CG for the solution of nonsymmetric linear system, *SIAM J. Aci. Stat. Comp.,* **13,** 631–644.
Vogel, C.R., 2002. *Computational Methods for Inverse Problems*, SIAM Frontiers in Applied Mathematics, pp. 129–150.
Wilt, M.J., Alumbaugh, D.L., Morrison, H.F., Becker, A., Lee, K.H. & Deszcz-Pan, M., 1995. Crosswell electromagnetic tomography: system design considerations and field results, *Geophysics,* **60,** 871–885.
Zhdanov, M.S. & Chernyak, V.V., 1987. An automated method of solving the two-dimensional inverse problem of electromagnetic induction within the Earth, *Transactions (Doklady) USSR Academy of Sciences, Earth Science Sections,* **296,** 59–63.
Zhdanov, M.S. & Yoshioka, K., 2003. Cross-well electromagnetic imaging in three dimensions, *Exploration Geophysics,* **34,** 34–40.
Zwamborn, A.P.M. & van den Berg, P.M., 1992. The three dimensional weak form of the conjugate gradient FFT method for solving scattering problems, *IEEE Transactions Microwave Theory and Techniques,* **40,** 1757–1766.

APPENDIX A: DISCRETIZATION PROCEDURE

We assume that the computational domain D is a rectangular domain with boundaries along the x_1 and x_3 directions. We discretize the domain D uniformly in rectangular subdomains of dimensions Δx_1 by Δx_3 with centre points located at:

$$x_{1;m} = x_{1;\frac{1}{2}} + (m-1)\Delta x_1, \quad m = 1, \ldots, M, \tag{A1}$$

$$x_{3;n} = x_{3;\frac{1}{2}} + (n-1)\Delta x_3, \quad n = 1, \ldots, N, \tag{A2}$$

in which $x_{1;1/2}$ and $x_{3;1/2}$ denote the lower left corner of the rectangle computation domain. In each subdomain, we assume the conductivity contrast χ to be constant and equal to the value at the centre point, namely, $\chi_{m,n} = \chi(x_{1,m}, x_{3,n})$. In this appendix we give the weighting procedure to discretize the gradient-divergence operator and the weakening procedure to obtain the discrete version of the normalized vector potential. Further, for completeness, the explicit expressions for the adjoint operators are also given.

A1 Weighting procedure

We define three sequences of basis functions over the domain D, namely, a sequence $\psi^{(1)}_{m,n,}(x_1, x_3)$ that is continuous in the x_1-direction and may allow jumps in the x_3-direction, a sequence $\psi^{(2)}_{m,n,}(x_1, x_3)$ that may allow jumps in both the x_1- and x_3-directions, and a sequence $\psi^{(3)}_{m,n,}(x_1, x_3)$ that may allow jumps in the x_3-direction and is continuous in the x_3-direction. The most simple basis functions, which meet these requirements are the rooftop functions Zwamborn & van den Berg (1992). In order to construct the rooftop functions that meet our objectives, we define two 1-D functions. The first is a piecewise constant function, namely, the pulse function, with support Δy, defined as

$$\Pi(y|\Delta y) = \begin{cases} 1 & \text{if } -\frac{1}{2}\Delta y < y < \frac{1}{2}\Delta y\,, \\ \frac{1}{2} & \text{if } |y| = \frac{1}{2}\Delta y\,, \\ 0 & \text{elsewhere}\,. \end{cases} \tag{A3}$$

The second is a piecewise linear and continuous function, namely, the triangle function, with support $2\Delta y$, defined as

$$\Lambda(y|,\Delta y) = \begin{cases} \left(1 + \frac{y}{\Delta y}\right) & \text{if } -\Delta y < y < 0\,, \\ \left(1 - \frac{y}{\Delta y}\right) & \text{if } 0 < y < \Delta y\,, \\ 0 & \text{elsewhere}\,. \end{cases} \tag{A4}$$

The expansion functions are now defined as

$$\begin{aligned} \psi^{(1)}_{m,n}(x_1, x_3) &= \Lambda(x_1 - x_{1;m}|\Delta x_1)\Pi(x_3 - x_{3;n}|\Delta x_3)\,, \\ \psi^{(2)}_{m,n}(x_1, x_3) &= \Pi(x_1 - x_{1;m}|\Delta x_1)\Pi(x_3 - x_{3;n}|\Delta x_3)\,, \\ \psi^{(3)}_{m,n}(x_1, x_3) &= \Pi(x_1 - x_{1;m}|\Delta x_1)\Lambda(x_3 - x_{3;n}|\Delta_{x_3})\,, \end{aligned} \tag{A5}$$

for $m = 1, \ldots, M$ and $n = 1, \ldots, N$. Let us further define the quantities

$$\tilde{\boldsymbol{E}}_{m,n} = \tilde{\boldsymbol{E}}(x_{1;m}, x_{3;n}, k_2)\,, \tag{A6}$$

$$\tilde{\boldsymbol{A}}_{m,n} = \tilde{\boldsymbol{A}}(x_{1;m}, x_{3;n}, k_2)\,. \tag{A7}$$

Then, (21) is discretized as

$$\tilde{\boldsymbol{E}}^{\text{inc}}_{m,n} = \tilde{\boldsymbol{E}}_{m,n} - k_0^2\tilde{\boldsymbol{A}}_{m,n} - [\tilde{\boldsymbol{\nabla}}\tilde{\boldsymbol{\nabla}}\cdot\tilde{\boldsymbol{A}}]_{m,n}, \tag{A8}$$

for $m = 1, \ldots, M$ and $n = 1, \ldots, N$. Using the expansion functions of (A5) each component of the last term of (A8) is replaced by its weak version as

$$[\tilde{\boldsymbol{\nabla}}\tilde{\boldsymbol{\nabla}}\cdot\tilde{\boldsymbol{A}}]_{\kappa;m,n} = \frac{\int_{x_1,x_3\in D}\psi^{(\kappa)}_{m,n}(x_1,x_3)\,[\tilde{\boldsymbol{\nabla}}\tilde{\boldsymbol{\nabla}}\cdot\tilde{\boldsymbol{A}}]_\kappa(x_1,x_3)\,dA}{\int_{x_1,x_3\in D}\psi^{(\kappa)}_{m,n}(x_1,x_3)\,dA}\,, \tag{A9}$$

while the component of the normalized vector potential $\tilde{\boldsymbol{A}}$ is expanded in a sequence of the basis functions, as follows

$$\tilde{A}_\kappa(x_1,x_3,k_2) = \sum_{q,r}\tilde{A}_{\kappa;q,r}\psi^{(\kappa)}_{q,r}(x_1,x_3), \quad \kappa = 1,2,3. \tag{A10}$$

We then arrive at

$$\begin{aligned}
[\tilde{\boldsymbol{\nabla}}\tilde{\boldsymbol{\nabla}}\cdot\tilde{\boldsymbol{A}}]_{1;m,n} &= \frac{\tilde{A}_{1;m+1,n} - 2\tilde{A}_{1;m,n} + \tilde{A}_{1;m-1,n}}{(\Delta x_1)^2} - \mathrm{i}k_2\frac{\tilde{A}_{2;m+1,n} - \tilde{A}_{2;m-1,n}}{2\Delta x_1} + \frac{\tilde{A}_{3;m-1,n-1} - \tilde{A}_{3;m-1,n+1} - \tilde{A}_{3;m+1,n-1} + \tilde{A}_{3;m+1,n+1}}{4\Delta x_1\Delta x_3},\\
[\tilde{\boldsymbol{\nabla}}\tilde{\boldsymbol{\nabla}}\cdot\tilde{\boldsymbol{A}}]_{2;m,n} &= -\mathrm{i}k_2\frac{\tilde{A}_{1;m+1,n} - \tilde{A}_{1;m-1,n}}{2\Delta x_1} - k_2^2\tilde{A}_{2;m,n} - \mathrm{i}k_2\frac{\tilde{A}_{3;m,n+1} - \tilde{A}_{3;m,n-1}}{2\Delta x_3},\\
[\tilde{\boldsymbol{\nabla}}\tilde{\boldsymbol{\nabla}}\cdot\tilde{\boldsymbol{A}}]_{3;m,n} &= \frac{\tilde{A}_{1;m-1,n-1} - \tilde{A}_{1;m-1,n+1} - \tilde{A}_{1;m+1,n-1} + \tilde{A}_{1;m+1,n+1}}{4\Delta x_1\Delta x_3} - \mathrm{i}k_2\frac{\tilde{A}_{2;m,n+1} - \tilde{A}_{2;m,n-1}}{2\Delta x_3} + \frac{\tilde{A}_{3;m,n+1,} - 2\tilde{A}_{3;m,n} + \tilde{A}_{3;m,n-1}}{(\Delta x_3)^2}.
\end{aligned} \tag{A11}$$

Note that the results in (A11) are identical to the ones if we had replaced (A9) directly by its finite-difference approximation Abramowitz & Stegun (1968).

A2 Weak form of the normalized vector potential

Next, we have to replace the continuous representation of the normalized vector potential $\tilde{\boldsymbol{A}}$ by a discrete one. In order to cope with the singularity of the Green function, we take the circular mean of the normalized vector potential in the 2-D Cartesian space. We integrate $\tilde{\boldsymbol{A}}$ over a circular domain in the Cartesian 2-D space with centre at the point $(x_{1;m}, x_{3;n})$ and with radius $a = \sqrt{\Delta x_1\Delta x_3/\pi}$. The results are divided by the circular area πa^2. Note that the latter area is equal to the area $\Delta x_1\Delta x_3$ of a rectangular sub domain We then may write for each component, $\kappa = 1, 2, 3$, of the vector potential

$$\tilde{A}_\kappa(x_{1;m}, x_{3;n}, k_2) = \frac{\int_{|\boldsymbol{x}''|<a}\tilde{A}_\kappa(x_{1;m}+x_1'', x_{3;n}+x_3'', k_2)\,dA}{\int_{|\boldsymbol{x}''|<a}dA} = \int_{x_1',x_2'\in D}\tilde{\mathcal{G}}(x_{1;m}-x_1', x_{3;n}-x_3', k_2)\chi(x_1',x_3')\tilde{E}_\kappa(x_1',x_3',k_2)\,dA\,, \tag{A12}$$

where we have interchanged the order of integrations, such that

$$\tilde{\mathcal{G}}(x_1,x_3,k_2) = \frac{\int_{[(x_1'')^2+(x_3'')^2]^{\frac{1}{2}}<a}\tilde{G}(x_1+x_1'', x_3+x_3'', k_2)\,dA}{\int_{[(x_1'')^2+(x_3'')^2]^{\frac{1}{2}}<a}dA}\,. \tag{A13}$$

Computation of the circular mean $\tilde{\mathcal{G}} = \tilde{\mathcal{G}}(x_1, x_3, k_2)$ leads to

$$\tilde{\mathcal{G}} = \begin{cases} \dfrac{i}{2k_0a}H_1^{(1)}(k_0a)J_0(k_0R) - \dfrac{1}{\pi(k_0a)^2}, & R \le a,\\[2ex] \dfrac{i}{2k_0a}J_1(k_0a)H_0^{(1)}(k_0R), & R \ge a, \end{cases} \tag{A14}$$

where the 2-D distance function R is given by

$$R(x_1,x_3) = \left(x_1^2 + x_3^2\right)^{\frac{1}{2}}. \tag{A15}$$

Note that, for the limiting case $a \to 0$, the weak form of the Green function, $\tilde{\mathcal{G}}$ in case $|\boldsymbol{x}| > a$, tends to its strong form $\tilde{G}$. In fact, $\tilde{\mathcal{G}}(x_1, x_3, k_2)$ is the mean value of the Green function over a circular domain with centre at (x_1, x_3). Note that this weakening of the singularity is different from the technique used by van Bladel (1991), where the spatial differentiations are acting on the Green function directly, while we compute first the normalized vector potential $\tilde{\boldsymbol{A}}$, in which the Green function has been weakened by taking its circular mean (Richmond 1965), and subsequently the differentiations are carried out numerically on the normalized vector potential $\tilde{\boldsymbol{A}}$. This technique has proven to yield an efficient, stable, and accurate algorithm. But note that the choices of discretization points in Zwamborn & van den Berg (1992) are far more complicated than the one used in Abubakar & van den Berg (2004).

After this weakening procedure, we are now able to compute the integral over D in (A12) numerically. In view of the functional properties of $\tilde{E}_\kappa$, we approximate the integral in (A12) using a midpoint rule. We then arrive at

$$\tilde{\boldsymbol{A}}_{m,n} = \tilde{\boldsymbol{A}}(x_{1;m}, x_{3;n}, k_2) = \Delta x_1\Delta x_3\sum_{m'=1}^{M}\sum_{n'=1}^{N}\tilde{\mathcal{G}}_{m-m',n-n'}\,\chi_{m',n'}\,\tilde{\boldsymbol{E}}_{m',n'}\,, \tag{A16}$$

for $m = 0, \ldots, M+1$ and $n = 0, \ldots, N+1$, where

$$\tilde{\mathcal{G}}_{m-m',n-n'} = \tilde{\mathcal{G}}(x_{1;m} - x_{1;m'}, x_{3;n} - x_{3;n'}, k_2)\,. \tag{A17}$$

Note that each component, $\tilde{A}_{\kappa;m,n}$, $\kappa = 1, 2, 3$, is a discrete convolution in m' and n', and can efficiently be computed by a 2-D fast Fourier transform (FFT) routine Press *et al.* (1992).

A3 Explicit expression of the adjoint operator

The adjoint operator $\tilde{\boldsymbol{G}}_D$ is defined through the relation

$$\langle \tilde{\boldsymbol{r}}, \tilde{\boldsymbol{G}}_D \chi \tilde{\boldsymbol{E}} \rangle_D = \langle \overline{\chi}\, \tilde{\boldsymbol{G}}_D^* \tilde{\boldsymbol{r}}, \tilde{\boldsymbol{E}} \rangle_D\,, \tag{A18}$$

where $\tilde{\boldsymbol{r}}$ and $\tilde{\boldsymbol{E}}$ are both in the same vector space, in domain D. Substituting the expression of the operator $\tilde{\boldsymbol{G}}_D \chi \tilde{\boldsymbol{E}}$ in the left-hand side of (A18) and interchanging the various summations, the adjoint operator $\tilde{\boldsymbol{G}}_D^*$ is recognized as

$$\left(\tilde{\boldsymbol{G}}_D^* \tilde{\boldsymbol{r}}\right)_{\kappa;m,n} = \Delta x_1 \Delta x_3 \sum_{m'=0}^{M+1} \sum_{n'=0}^{N+1} \tilde{\mathcal{G}}_{m'-m,n'-n} \tilde{F}_{\kappa;m',n'}\,, \tag{A19}$$

for $m = 1, \ldots, M$ and $n = 1, \ldots, N$, where

$$\begin{aligned}
\tilde{F}_{1;m,n} &= \overline{k_0^2}\, \tilde{r}_{1;m,n} + \frac{\tilde{r}_{1;m-1,n} - 2\tilde{r}_{1;m,n} + \tilde{r}_{1;m+1,n}}{(\Delta x_1)^2} + \mathrm{i}k_2 \frac{\tilde{r}_{2;m-1,n} - \tilde{r}_{2;m+1,n}}{2\Delta x_1} + \frac{\tilde{r}_{3;m+1,n} - \tilde{r}_{3;m+1,n} - \tilde{r}_{3;m-1,n} + \tilde{r}_{3;m-1,n}}{4\Delta x_1 \Delta x_3}, \\
\tilde{F}_{2;m,n} &= \overline{k_0^2}\, \tilde{r}_{2;m,n} + \frac{\tilde{r}_{1,m+1,n+1} - \tilde{r}_{1;m+1,n-1} - \tilde{r}_{1;m-1,n+1} + \tilde{r}_{1;m-1,n-1}}{4\Delta x_1 \Delta x_2} + k_2^2\, \tilde{r}_{2;m,n} + \mathrm{i}k_2 \frac{\tilde{r}_{3;m,n-1} - \tilde{r}_{3;m,n+1}}{2\Delta x_3}, \\
\tilde{F}_{3;m,n} &= \overline{k_0^2}\, \tilde{r}_{3;m,n} + \frac{\tilde{r}_{1;m+1,n} - \tilde{r}_{1;m+1,n} - \tilde{r}_{1;m-1,n} + \tilde{r}_{1;m-1,n}}{4\Delta x_1 \Delta x_3} + \mathrm{i}k_2 \frac{\tilde{r}_{2;m,n-1} - \tilde{r}_{2;m,n+1}}{2\Delta x_3} + \frac{\tilde{r}_{3;m,n+1} - 2\tilde{r}_{3;m,n} + \tilde{r}_{3;m,n-1}}{(\Delta x_3)^2}.
\end{aligned} \tag{A20}$$

Since according to (A19) m' runs from 0 to $M+1$ and n' runs from 0 to $N+1$, we set in the expressions of (A20)

$$\begin{aligned}
&\tilde{r}_{\kappa m,n} = 0\,, \quad m = -1, 0, M+1, M+2\,, \quad \forall n, \\
&\tilde{r}_{\kappa m,n} = 0\,, \quad n = -1, 0, N+1, N+2\,, \quad \forall m.
\end{aligned} \tag{A21}$$

Note that $(\tilde{\boldsymbol{G}}_D^* \tilde{\boldsymbol{r}})_{\kappa m,n}$ are discrete convolutions in m' and n', and these convolutions can be computed efficiently by 2-D FFT routines (Press *et al.* 1992).